batteries

MDPI

Article

Lévy Jump Nonlocal SPDE and BA-PINN Modeling for Battery Fracture and Thermal-Runaway Warning

Yongfang Zhu [1,*], Qing Xie [2] and Jingli Jia [2]

[1] Faculty of Engineering, Anhui Sanlian University, Hefei 230601, China
[2] School of Liberal Studies, Anhui Wenda University of Information Engineering, Hefei 231201, China; xieqing@mail.wenda.edu.cn (Q.X.); jiajingli@mail.wenda.edu.cn (J.J.)
* Correspondence: zyf@mail.slu.edu.cn

Abstract

Electrode-particle fracture and thermal runaway remain major safety and durability challenges for lithium-ion batteries. Deterministic degradation models are limited in representing random crack nucleation, long-range crack interactions, and critical transitions from stable operation to failure. A computational framework is proposed that combines a Lévy-jump-driven nonlocal stochastic partial differential equation (SPDE) model with a Bifurcation-Aware Physics-Informed Neural Network (BA-PINN). The framework couples fractional diffusion, peridynamic damage evolution, thermal feedback, state-space eigenvalue tracking, and damage-variance monitoring. Evaluation is conducted on controlled synthetic fracture simulations, Oxford battery cycling records, and open-access abuse-test records from the Battery Failure Databank. The damage-field results are interpreted as numerical consistency and surrogate-learning evidence, with direct experimental crack-map validation remaining outside the present dataset scope. On the simulated fracture dataset, the proposed method obtains a damage-field mean squared error of 0.023 ± 0.002 and a structural similarity index of 0.962 ± 0.006. For the evaluated thermal-runaway warning task, it achieves an AUC-ROC of 0.987 ± 0.004 and an average model-inferred warning lead time of 5.2 ± 0.2 h. These results demonstrate the methodological feasibility of combining stochastic nonlocal fracture modeling with bifurcation-aware learning. However, broader validation remains necessary, particularly using particle-resolved experiments and larger event-level thermal-runaway datasets.

Keywords: lithium-ion battery; electrode particle fracture; Lévy jump SPDE; nonlocal damage modeling; bifurcation-aware PINN; thermal runaway early warning

Academic Editor: Xianglin Li

Received: 5 June 2026
Revised: 7 July 2026
Accepted: 8 July 2026
Published: 12 July 2026

1. Introduction

Lithium-ion batteries are widely used in electric vehicles, portable electronics, new-energy facilities, and power plants. Their broad adoption is driven by high energy density, improved cycle life, and continuing advances in materials and system-level integration [1,2]. Electrochemical degradation, mechanical damage, and other material-dependent failure mechanisms after many cycles also reduce the service life and safety of the battery, especially in conditions of high-rate or high-temperature operation and mechanical stress [3,4]. Among the main failure modes, particle fracture is a major degradation pathway. It is driven by lithium concentration gradients, stress accumulation, and micro-

structural damage. Particle fracture accelerates capacity fade, exposes fresh reactive surfaces, and may trigger thermal instability under extreme operating conditions [5,6]. Thermal runaway is a type of self-accelerating heat release and a cascade of electrochemical side reactions that can lead to fire or explosion; thus, it remains a major safety issue for large-scale deployment of lithium-ion batteries [7,8].

Stochasticity and Nonlocality of Electrode Particle Fracture**:** The fracture process of battery electrode particles is inherently random and results from a combination of microstructural defects, non-uniform lithiation paths, and the probability of crack initiation and propagation in these particles [9,10]. Traditional deterministic models, such as Fickian diffusion equations and classical continuum damage mechanics, assume a smooth, predictable degradation path and are unable to account for sudden, catastrophic crack events that have been observed experimentally [11]. Fractures in brittle electrode materials (such as silicon and high-nickel cathodes) are also nonlocal; that is, a crack nucleus at one place can cause stress redistribution and subsequent cracking at a distant location through long-range elastic interactions [12,13]. Therefore, this nonlocality is in conflict with the local differential operators of the conventional PDE model.

Limitations of Existing Physics-Informed Machine Learning Approaches: Physics-informed neural networks (PINNs) have shown excellent results in solving forward and inverse problems for PDEs, such as battery degradation modelling [14,15]. Standard PINN formulations have several deficiencies in their application to the prediction of fracture and thermal runaway. First, vanilla PINNs are built based on deterministic governing equations and cannot model the stochastic behavior of random crack nucleation and propagation [16]. Second, they use local differential operators that are not suitable for capturing nonlocal fracture interactions [17]. Third, the current data-driven governing-equation discovery frameworks focus on identifying dynamical laws or reduced coordinates and do not explicitly integrate bifurcation-aware early-warning mechanisms [18,19]. Fourth, most existing studies lack an explicit early-warning function and can only forecast state-variable changes rather than detect severe deviations before failure.

Bifurcation Dynamics of Thermal Runaway: The transition to thermal runaway is, in fact, a bifurcation phenomenon [20,21]. As the internal temperature rises, so too does the speed of exothermic decomposition; therefore, a positive feedback loop is formed. At a certain value of the parameter, the stable operating equilibrium loses stability via a fold bifurcation (saddle-node), and the system jumps to a high-temperature attracting state from which recovery cannot be achieved [22]. To detect the approach of this bifurcation, one can identify critical slowing down and increased variance that occur just before it and thus provide an early warning signal [23,24]. Although neural-network-based surrogate models have recently been explored for bifurcation analysis in structural mechanics, computational fluid dynamics, and nonlinear PDE systems, their integration with stochastic nonlocal electrode-particle damage modeling for lithium-ion battery thermal-runaway early warning remains limited.

Recent battery-specific studies have analyzed lithium-ion battery spontaneous combustion and thermal-runaway critical heating using bifurcation or critical-parameter frameworks [25,26]. In situ thermal-runaway imaging has also shown abrupt internal failure evolution during heating [27], providing phenomenological evidence of rapid internal transition. In the present work, the fold-bifurcation framework serves as a reduced-order stability description of heat-generation/heat-removal imbalance, with abuse-trajectory heterogeneity retained as an explicit modeling limitation.

To address the above problems, this paper introduces a computational framework for stochastic nonlocal damage modelling and bifurcation-aware thermal runaway warning. The four contributions are as follows:

1. Lévy Jump Nonlocal SPDE System: A coupled system of stochastic partial differential equations driven by Lévy jump processes is derived to model the interactions among lithium concentration diffusion, mechanical deformation, nonlocal damage evolution, and thermal feedback in electrode particles. The Lévy jump component captures sudden, discontinuous damage events (microcracking) that fall outside a Gaussian stochastic representation.
2. Fractional Nonlocal Integral Operator: A nonlocal integral operator based on fractional calculus and peridynamic theory is formulated to quantify long-range damage interactions across a finite horizon. This operator generalizes classical peridynamics by incorporating fractional-order interactions with Lévy-stable jump measures.
3. Bifurcation-Aware PINN (BA-PINN): We develop a specialized physics-informed neural-network architecture with three functions. It tracks solution branches by pseudo-arc-length continuation, detects bifurcations through eigenvalue analysis of the linearized physical residual operator, and increases the training weight for bifurcation-proximal samples as critical parameter values are approached.
4. Damage Variance Early Warning: We establish a damage-variance monitoring scheme that tracks the spatial heterogeneity of the predicted damage field and provides model-inferred early-warning signals with quantified lead times prior to thermal-runaway onset under the evaluated abuse-test protocol.

Through experimental evaluation across synthetic fracture simulations, cycling degradation records, and open-access abuse-test data, we show that the proposed framework improves damage-field prediction and thermal-runaway warning performance under the evaluated settings.

2. Related Work

This work sits at the intersection of battery degradation modeling, peridynamic fracture mechanics, stochastic partial differential equations, physics-informed machine learning, and bifurcation theory. We review these research areas in sequence and clarify how the proposed framework extends prior studies.

Battery Degradation and Particle Fracture Modeling: The mechanical degradation of lithium-ion battery electrodes has been extensively studied through continuum and mesoscale models. Doyle, Fuller, and Newman [28] established a foundational pseudo-two-dimensional (P2D) model for battery electrochemistry, which has been subsequently extended to include mechanical stress coupling [29]. Christensen and Newman [30] first incorporated stress generation due to lithium intercalation into the P2D framework, while Zhang et al. [31] developed analytical stress solutions for spherical electrode particles. Woodford, Chiang, and Carter [32] demonstrated that dimensionless parameters controlling mechanical degradation can be extracted from electrochemical measurements. More recently, Tu et al. [33] developed a coupled chemo-mechano-damage phase-field framework for modeling cracking, interface debonding, and capacity fade in core–shell cathode particles for lithium-ion batteries, providing a more recent reference for phase-field fracture modeling in battery electrode materials. Ai, Wu, and Martínez-Pañeda [34] developed a coupled phase-field formulation for modelling fatigue cracking in lithium-ion battery electrode particles. However, these deterministic models do not account for the stochastic nature of crack nucleation or the nonlocal interactions between crack sites.

Peridynamics and Nonlocal Fracture Mechanics: Silling [35] proposed peridynamics (PD) as a nonlocal reformulation of continuum mechanics that is suitable for discontinuities such as cracks. In PD, the classical stress-divergence operator is replaced by an integral balance over a finite spatial horizon, so crack initiation and growth can be represented through bond failure without imposing an additional local crack-tip criterion. Silling and Askari [36] showed that PD can represent complex fracture patterns. Macek and Silling

[37] developed a finite-element-based implementation of peridynamics, and Oterkus, Madenci, and Agwai [38] extended peridynamic theory to thermal diffusion problems. Wang and Tong [39] developed a coupled chemo-mechanical peridynamic model for delayed fracture in electrodes during lithiation, and Wang et al. [40] studied three-dimensional fracture evolution during lithiation in a peridynamic framework. Most PD-based battery models remain deterministic and omit stochastic jump forcing or fractional-order nonlocal interactions.

Stochastic Partial Differential Equations with Jumps: Models of random phenomena in physical systems using SPDEs have been developed considerably. Peszat and Zabczyk [41] present an all-encompassing study of SPDEs driven by Lévy processes, and Applebaum [42] covers the broader theory of Lévy processes and stochastic calculus. Xie [43] studied sharp heat kernel estimates for fractional Laplacian perturbations with gradient terms. Biccari, Warma, and Zuazua [44] obtained local elliptic regularity results for the Dirichlet fractional Laplacian and thus provided a mathematical basis for the regularity analysis of fractional nonlocal operators. Lévy-driven SPDEs have been used in finance, turbulence, and anomalous diffusion, while applications to battery electrode fracture remain limited.

Physics-Informed Neural Networks: Raissi, Perdikaris, and Karniadakis introduced PINNs as a framework for encoding physical laws into neural network training through PDE-based loss functions. Subsequent developments include XPINNs for domain decomposition [45], cPINNs for conservative formulations [46], and hp-VPINNs for variational problems [47]. PINNs have been applied to battery modeling: Wang et al. [48] developed a physics-informed neural network for stable lithium-ion battery degradation modeling and prognosis, while Zheng, Yin, and Zhang [49] introduced physics-informed deep operator networks for electrochemical state-space modeling of Li-ion batteries.

However, standard PINN formulations do not handle stochastic equations, nonlocal operators, or bifurcation phenomena.

Recent reviews on machine-learning-assisted multiscale design of energy materials further highlight the role of machine learning interatomic potentials, microstructure reconstruction, and physics-informed PDE solvers in connecting atomistic, microstructural, and continuum-scale modeling [50]. This broader multiscale learning context supports the use of physics-informed surrogate models for battery degradation analysis, while particle-resolved fracture evidence remains necessary for calibrating stochastic crack-evolution assumptions.

Bifurcation Detection and Early Warning: Critical transitions in dynamical systems are preceded by generic early warning signals, including increased autocorrelation, variance, and skewness. In the battery domain, Gu et al. [51] proposed a state-of-safety-based early warning method for lithium-ion battery thermal runaway, while Goswami et al. [52] integrated multiphysics modeling and machine learning for thermal runaway prediction in lithium-ion battery modules. More recently, Chen et al. [53] proposed a data-driven early warning framework for thermal runaway in energy storage batteries by combining reconstruction-error-based anomaly detection, Bi-LSTM feature extraction, attention mechanisms, and ensemble learning, which provides a more recent benchmark for data-driven thermal runaway warning. Kim et al. [54] developed a multiphysics-informed neural network for modeling and predicting lithium-ion battery thermal runaway. However, none of these approaches combine bifurcation-aware training with physics-informed neural networks or leverage nonlocal damage field variance as an early warning indicator.

Recent battery-safety studies have also emphasized physics-guided warning, multimodal thermal-runaway prediction, and data-driven early-warning models [51–56]. In this context, the present framework is evaluated as a model-inferred coupling of a latent

nonlocal damage field with bifurcation-aware state-space monitoring and remains complementary to direct calorimetry-based safety testing and particle-resolved imaging validation.

Comparison with Existing Approaches: Table 1 provides a comprehensive comparison of our method against seven representative baseline approaches across six key capabilities.

Table 1. Comparison with existing methods.

Method	Stochastic Damage	Nonlocal Fracture	Lévy Jumps	Bifurcation Awareness	Physics-Informed	Early Warning
Peridynamics [35]	×	✓	×	×	✓	×
Phase-Field [33]	×	×	×	×	✓	×
Vanilla PINN [14]	×	×	×	×	✓	×
XPINN [45]	×	×	×	×	✓	×
T-RUNSAFE [56]	×	×	×	×	×	✓
State-of-the-art EWS [51]	×	×	×	×	×	✓
PIARN [55]	×	×	×	×	✓	✓
Ours	✓	✓	✓	✓	✓	✓

Note: In Table 1, the check mark (✓) indicates that the corresponding method explicitly includes or supports the listed capability, whereas the cross mark (×) indicates that the capability is absent or not explicitly incorporated in that method.

Table 1 summarizes how the proposed framework differs from representative fracture, PINN, and early-warning methods in model scope and key capabilities. Existing fracture models provide physical interpretability, but they generally lack stochastic jump forcing and warning functions. In contrast, existing early-warning models focus on cell-level risk indicators and do not explicitly model the evolution of nonlocal spatial damage. Thus, the proposed framework connects stochastic nonlocal fracture modeling and bifurcation-aware warning through a latent damage-field representation.

3. Preliminaries

This section summarizes the mathematical foundations used by the proposed framework: Lévy processes, fractional calculus, peridynamic theory, physics-informed neural networks, and bifurcation theory. These concepts support the coupled SPDE system and the BA-PINN architecture introduced in Section 4.

Lévy Processes and Stable Distributions: A Lévy process $\{L_t\}_{t\geq 0}$ is a stochastically continuous process with stationary and independent increments that satisfies L0 = 0 almost surely. The Lévy–Khintchine representation expresses such processes in terms of their Lévy measure ν, which indicates the expected number of jumps of a certain size per unit of time. For the class of stable Lévy processes with stability index $\alpha \in (0,2)$, the Lévy measure has the following special form:

$$\nu_\alpha(dz) = C_\alpha |z|^{-1-\alpha} dz \tag{1}$$

where C_α is a normalisation constant that depends on the dimension and stability index. This power-law measure has a heavy tail and a Pareto index α; therefore, large jumps occur with a non-negligible probability, and a Gaussian process cannot be used to model these catastrophic crack events. The corresponding characteristic function of a general α-stable distribution is as follows:

$$\varphi_\xi(u) = \exp\left(-|u|^\alpha \left(1 - i\beta \,\mathrm{sgn}(u) \tan\frac{\pi\alpha}{2}\right)\right) \tag{2}$$

where $\beta \in [-1,1]$ controls the skewness of the distribution. The stability parameter α governs the tail heaviness: As $\alpha \to 2$, the distribution approaches Gaussianity, while

smaller values of α correspond to increasingly frequent large jumps. In the context of electrode particle fracture, empirical evidence suggests that $\alpha \approx 1.5$ provides a good match for the distribution of microcrack sizes observed experimentally, reflecting the heterogeneous microstructure of battery electrode materials.

For the selected working value of α = 1.5, recent particle-resolved and cell-level evidence in silicon-based anodes provides experimental motivation for jump-type stochastic damage increments, including operando X-ray computed microtomography of channel and interfacial cracks in silicon anode solid-state batteries [57] and abrupt degradation observations in silicon-based lithium-ion cells [58]. These studies motivate the representation of fracture evolution as intermittent and heterogeneous, while the heavy-tailed Lévy form and the exact stability index remain calibrated, material-dependent modeling choices.

Fractional Laplacian and Nonlocal Diffusion: The fractional Laplacian $(-\Delta)^{\alpha/2}$ is the infinitesimal generator of the α-stable Lévy process and can be viewed as a type of nonlocal extension of traditional diffusion. For a function u on $\mathbb{R}^d$, the fractional Laplacian is defined by the following singular integral:

$$(-\Delta)^{\alpha/2}u(x) = C_{d,\alpha}\int_{\mathbb{R}^d}\frac{u(x)-u(y)}{|x-y|^{d+\alpha}}dy \tag{3}$$

where $C_{d,\alpha}$ is a normalization constant ensuring consistency with the Fourier-domain definition $\mathcal{F}\left[(-\Delta)^{\alpha/2}u\right](\xi) = |\xi|^{\alpha}\hat{u}(\xi)$. The singular integral representation in Equation (3) reveals the essential nonlocality of the operator: the value $(-\Delta)^{\alpha/2}u(x)$ depends on $u(y)$ for all $y \in \mathbb{R}^d$, with the influence of distant points decaying as a power law $|x-y|^{-(d+\alpha)}$. This long-range interaction kernel provides a natural way to model nonlocal damage accumulation in battery electrode particles; that is, stress redistribution at a crack site can affect regions far away from that site.

Peridynamic Theory: Peridynamics reformulates continuum mechanics by replacing the divergence of stress (a local differential operator) with an integral operator defined over a finite horizon δ. The equation of motion in the peridynamic formulation is

$$\rho(x)\ddot{u}(x,t) = \int_{B_\delta(x)} f\left(u(x',t)-u(x,t),x'-x\right)dV_{x'} + b(x,t) \tag{4}$$

where H(x) denotes the spherical neighborhood of radius δ centered at x, f (·) is the pairwise force function specifying the interaction between material points, and b(x, t) represents body forces. This nonlocal integral form avoids spatial derivatives at discontinuities and permits crack initiation through bond degradation once the stretch exceeds the critical value. The damage variable in bond-based peridynamics is the extent of material damage:

$$\mu(x,t) = 1 - \frac{\int_{B_\delta(x)}\omega\left(|x'-x|\right)\cdot\mathbb{1}_{[s(x',t)<s_0]}dV_{x'}}{\int_{B_\delta(x)}\omega\left(|x'-x|\right)dV_{x'}} \tag{5}$$

where the influence function weights neighboring material points, and the indicator term equals one for bonds that remain intact, i.e., bonds for which their stretch is below the critical value. Consequently, Equation (5) defines damage as one minus the normalized intact-bond fraction: The value approaches 0 for an intact neighborhood and approaches 1 when most bonds in the horizon have failed. This convention is used consistently in the subsequent damage-evolution and variance-monitoring analysis.

Physics-Informed Neural Networks: A PINN parametrizes the solution $u(x,t)$ of a PDE by a neural network $u_\theta(x,t)$ and trains the network parameters θ by minimizing a composite loss function that penalizes the PDE residual, boundary condition violation, and data misfit:

$$\mathcal{L}_{\text{PINN}} = \mathcal{L}_{\text{pde}} + \mathcal{L}_{\text{bc}} + \mathcal{L}_{\text{data}} \tag{6}$$

where $\mathcal{L}_{\text{pde}}$ measures the squared residual of the governing equation at collocation points, $\mathcal{L}_{\text{bc}}$ enforces boundary and initial conditions, and $\mathcal{L}_{\text{data}}$ fits available observational data. While PINNs have demonstrated impressive results for deterministic forward and inverse problems, the standard formulation in Equation (6) does not accommodate stochastic forcing, nonlocal operators, or the detection of bifurcation points in the solution manifold.

Bifurcation Theory: Bifurcations are qualitative changes in the behavior of a dynamical system that occur as parameters cross critical thresholds. The fold (saddle-node) bifurcation, described by the normal form

$$\dot{x} = \lambda - x^2 \tag{7}$$

captures the collision and annihilation of two equilibrium points as the control parameter λ passes through zero. For $\lambda > 0$, a stable and an unstable equilibrium coexist; for $\lambda < 0$, no equilibria remain, and trajectories diverge to infinity—a scenario that directly models the loss of stable operation preceding thermal runaway. The Hopf bifurcation, described in polar coordinates by

$$\dot{r} = \lambda r - r^3 \tag{8}$$

corresponds to the birth of a limit cycle from an equilibrium as λ increases through zero, modeling the onset of oscillatory thermal behavior that can precede runaway. Both bifurcation types exhibit critical slowing down, meaning that decay rates vanish near the bifurcation point. In stochastic systems, this behavior appears as increased variance and autocorrelation. These signals provide the theoretical basis for the proposed damage-variance early-warning scheme.

4. Methodology

This section presents the methodological core of the framework. The Lévy jump-driven nonlocal SPDE system for coupled electrochemical–mechanical–thermal degradation is introduced in Section 4.1, followed by the fractional nonlocal integral operator for long-range damage interactions in Section 4.2, the Bifurcation-Aware PINN architecture in Section 4.3, and the two-stage training strategy with damage variance monitoring in Section 4.4.

4.1. Lévy Jump Nonlocal SPDE System

We formulate a coupled system of stochastic partial differential equations that models the interplay among lithium concentration diffusion, mechanical deformation, nonlocal damage evolution, and thermal feedback in a representative electrode particle. The system comprises four coupled equations.

Lithium Concentration Diffusion: The lithium concentration field $c(x,t)$ evolves according to a fractional diffusion equation with drift coupling to the damage gradient and Langevin forcing:

$$\frac{\partial c}{\partial t} = D_\alpha(-\Delta)^{\alpha/2}c + \nabla\cdot(c\nabla\mu) + f_c(c,T) + \sigma_c\dot{W}_c \tag{9}$$

where D_α is the fractional diffusion coefficient (incorporating anomalous transport due to trapping at crack surfaces), $(-\Delta)^{\alpha/2}$ is the fractional Laplacian defined in Equation (3), the drift term $\nabla\cdot(c\nabla\mu)$ captures lithium flux toward damaged regions, $f_c(c,T)$ is the temperature-dependent reaction source term, and $\sigma_c\dot{W}_c$ represents Gaussian white noise modeling random concentration fluctuations. The fractional diffusion term in Equation (9) generalizes Fick's law to account for the anomalous subdiffusion observed in cracked electrode particles, where the mean squared displacement of lithium ions scales as $\langle x^2(t)\rangle \sim t^{2/\alpha}$ rather than linearly in time.

Mechanical Equilibrium: The mechanical displacement field $u(x,t)$ satisfies a wave equation with effective stress divergence, damage-dependent body forces, and Lévy jump forcing:

$$\rho \frac{\partial^2 u}{\partial t^2} = \nabla \cdot \sigma^{\text{eff}} + b(u,\mu) + \sigma_u \int_{\mathbb{R}^d} z\, \widetilde{N}(dt,dz) \tag{10}$$

where ρ is the material density, $\sigma^{\text{eff}} = (1-\mu)\sigma$ is the effective stress degraded by the damage field, $b(u,\mu)$ is the damage-dependent body force, and the compensated Poisson random measure integral $\sigma_u \int z\widetilde{N}(dt,dz)$ introduces Lévy jump forcing that models sudden mechanical perturbations from microcracking events. The Lévy jump term in Equation (10) complements the Gaussian white-noise forcing in Equation (9) by representing abrupt fracture-induced stress changes outside a purely Gaussian fluctuation model.

Nonlocal Damage Evolution: The damage field $\mu(x,t)$ evolves according to a fractional reaction-diffusion equation driven by Lévy-stable jump noise:

$$\frac{\partial \mu}{\partial t} = \mathcal{L}_\delta^{\text{NL}}[\mu] + g(\sigma^{\text{vm}},\mu) + \int_{\mathbb{R}} z\, N_\alpha(dt,dz) \tag{11}$$

Here, the nonlocal integral operator is defined in Section 4.2. The reaction term drives damage growth as a function of the von Mises equivalent stress. The Lévy-stable stochastic integral introduces heavy-tailed random jumps associated with large crack events. The operator in Equation (11) captures nonlocal damage accumulation through long-range interactions, while the Lévy jump term represents sudden damage increments corresponding to primary crack nucleation events.

Thermal Feedback: The temperature field $T(x,t)$ evolves according to the heat equation with reaction and Ohmic heating sources:

$$\rho C_p \frac{\partial T}{\partial t} = k\Delta T + Q_{\text{rxn}}(c,T) + Q_{\text{ohm}}(\sigma) \tag{12}$$

where ρC_p is the volumetric heat capacity, k is the thermal conductivity, $Q_{\text{rxn}}(c,T)$ is the exothermic reaction heat generated by SEI decomposition and electrolyte oxidation, and $Q_{\text{ohm}}(\sigma) = \sigma^{\text{eff}} : \dot{\varepsilon}$ is the Ohmic heating rate. Damage and temperature are bidirectionally coupled. Damage reduces effective thermal conductivity and increases Ohmic heating, while elevated temperature accelerates damage growth by increasing reaction rates. This positive feedback can drive thermal runaway.

Compound Poisson Representation of Lévy Forcing: The Lévy jump components in Equations (10) and (11) admit a compound Poisson representation that facilitates numerical implementation:

$$J(x,t) = \sum_{i=1}^{N(t)} Z_i\, \delta(x - X_i) \tag{13}$$

where $N(t)$ is a Poisson process with intensity λ_{jump} counting the number of crack events up to time t, $\{Z_i\}_{i\geq 1}$ denotes independent and identically distributed (i.i.d.) random variables drawn from the jump size distribution $\nu_\alpha/\nu_\alpha(\mathbb{R})$, and $\{X_i\}_{i\geq 1}$ denotes the spatial locations of crack events. This form indicates that crack events are a spatiotemporal Poisson point process with random intensities and spatial locations; thus, a statistically grounded model for the stochastic fracture process observed experimentally has been obtained.

Fractional Diffusion-Reaction-Damage Equation: Combining the nonlocal operator with the jump process yields the unified fractional diffusion-reaction-damage equation:

$$\frac{\partial \mu}{\partial t} = -(-\Delta)^{\alpha/2}\mu + \lambda_{\text{jump}} \int_{\mathbb{R}} [\mu(x+z,t) - \mu(x,t)]\, \nu_\alpha(dz) + R(\sigma^{\text{vm}},\mu) \tag{14}$$

The first term $-(-\Delta)^{\alpha/2}\mu$ in Equation (14) governs fractional diffusion of damage with long-range anomalous transport. The second term is the Lévy jump integral modeling discontinuous damage increments from crack events, and the third term $R(\sigma^{\text{vm}},\mu)$

captures local damage growth driven by stress. The competition between fractional diffusion (smoothing) and jump-driven nucleation (roughness) determines the fractal character of the damage field, consistent with experimental observations of crack surface roughness in battery electrodes.

Physical Closures and Boundary/Initial Conditions: The reaction source, damage-growth function, effective stress relation, heat-generation terms, and initial fields used in the coupled SPDE are defined in Equation (15). The synthetic particle simulations use no-flux concentration boundaries, traction-free mechanical boundaries, and convective thermal boundaries. These closures specify the reproducible numerical experiment and remain separate from chemistry-specific abuse models.

$$\begin{gathered} R_c(c,T) = k_c \exp\left(-E_c/(RT)\right) c(1-c) \\ G(\sigma_{vm},T,\mu) = A_d \exp\left(-E_d/(RT)\right) \max(\sigma_{vm}-\sigma_c,0)^m (1-\mu) \\ \sigma_{eff} = (1-\mu)^2 \mathrm{C}\colon(\varepsilon-\varepsilon_{Li}) \\ Q_{rxn}(T,\mu) = \sum_r H_r A_r \exp\left(-E_r/(RT)\right)\chi_r, \quad Q_{ohm} = I^2 R_{int}(\mu,T) \\ c(x,0) = c_0 + \xi_c(x), \quad \mu(x,0) = \mu_0 + \xi_\mu(x), \quad u(x,0) = 0, \quad T(x,0) = T_{amb} \end{gathered} \tag{15}$$

4.2. Fractional Nonlocal Integral Operator

We formulate a generalized nonlocal integral operator that combines fractional calculus with peridynamic horizon constraints, capturing long-range damage interactions beyond the classical peridynamic formulation.

Operator Definition: The fractional nonlocal integral operator is defined as

$$\mathcal{L}_\delta^{\mathrm{NL}}[\mu](x,t) = \int_{B_\delta(x)} \frac{\mu(x',t)-\mu(x,t)}{|x'-x|^{1+\alpha}} K_\delta(|x'-x|)\,dx' \tag{16}$$

where $B_\delta(x)$ is the horizon neighborhood of radius δ, $|x'-x|^{-(1+\alpha)}$ is the fractional interaction kernel with stability index α, and $K_\delta(r) = (\delta-r)^2/\delta^2$ is a horizon-modulating kernel that smoothly attenuates interactions near the horizon boundary. The operator in Equation (16) generalizes classical peridynamics (which corresponds to =1 with a constant kernel) to fractional-order interactions that capture the heavy-tailed spatial correlations of damage observed in heterogeneous electrode materials. As $\alpha \to 2$, the operator localizes to a second-order differential operator, recovering classical damage mechanics. For $\alpha \in (0,2)$, the operator exhibits the nonlocal scaling properties characteristic of fractional equations. To clarify the components of the proposed fractional nonlocal damage representation, Figure 1 first visualizes the fractional kernel, a representative Lévy jump trajectory, and the spatially varying horizon function.

Figure 1 shows the main components of the proposed fractional nonlocal damage representation. As shown in Figure 1a, decreasing α from 2.0 to 1.2 produces a heavier-tailed kernel and therefore increases sensitivity to long-range interactions within the peridynamic horizon. Figure 1b illustrates a discontinuous Lévy jump trajectory used to represent sudden microcrack nucleation and damage bursts. Figure 1c shows the spatially varying horizon function δ(x), which allows the nonlocal interaction range to vary across the electrode-particle domain. Together, these components provide the stochastic, nonlocal, and spatially adaptive basis of the fracture model introduced in Section 4.

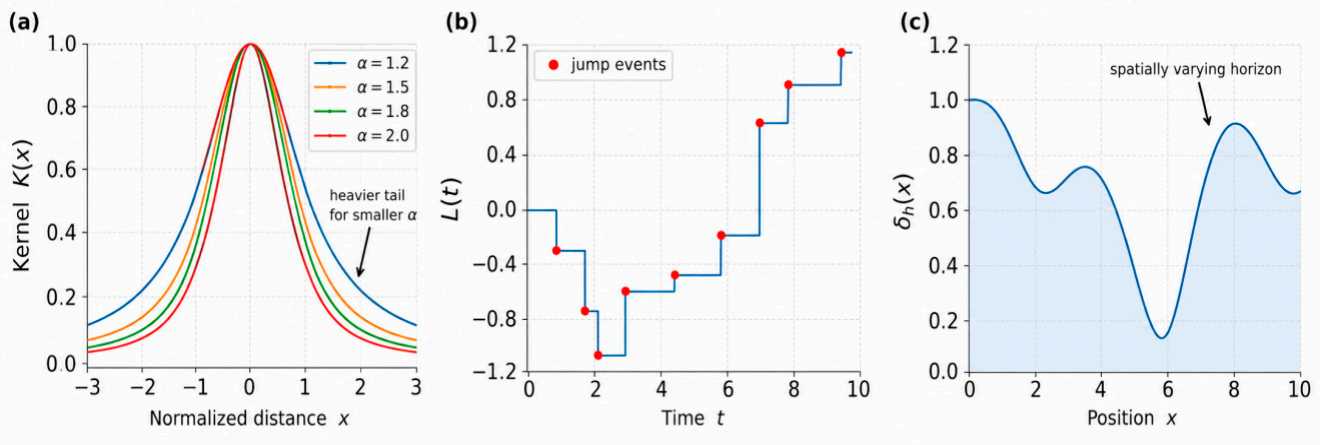

Figure 1. Conceptual schematic of the fractional nonlocal modeling components. (**a**) Fractional nonlocal kernel for varying stability index α, showing increasingly heavy-tailed interactions as α decreases. (**b**) Representative Lévy jump trajectory, where the blue step line represents the cumulative Lévy jump process L(t), and the red markers indicate individual jump events. (**c**) Spatially varying horizon function δ(x), which modulates the nonlocal interaction range across the particle domain.

4.3. Bifurcation-Aware PINN Architecture

The Bifurcation-Aware PINN (BA-PINN) is introduced as an extension of the standard PINN framework that incorporates bifurcation detection, pseudo-arc-length branch tracking, and damage-variance-based critical-transition monitoring.

4.3.1. Overall Framework

The BA-PINN parameterizes the solution fields (c, u, μ, T) of the coupled SPDE system (Equations (9)–(12)) with deep neural networks and trains them using a composite loss function that includes the PDE residual, boundary conditions, data fitting, and a novel bifurcation awareness term. The system contains three submodules: the physics network, the bifurcation module, and the monitoring module. The physics network enforces the SPDE residuals, the bifurcation module tracks eigenvalues of the linearized physical residual operator, and the monitoring module computes damage variance for early warning. Before discussing the training procedure, Figure 2 provides an overview of the BA-PINN architecture and the information flow among the physics, bifurcation, and monitoring modules.

Figure 2 summarizes the BA-PINN structure. The physics network receives spatial coordinates x and time t and outputs the concentration, displacement, damage, and temperature fields. Automatic differentiation and FFT-based nonlocal operators are then used to compute the SPDE residuals. The bifurcation module linearizes the learned physical residual with respect to the state variables and tracks its leading eigenvalues as the control parameter changes. A leading real eigenvalue approaching zero is treated as a fold-type instability indicator, whereas a complex-conjugate eigenvalue pair crossing the imaginary axis is treated as a Hopf-type instability indicator. Stability analysis is therefore associated with the physical state space and separated from neural-network parameter-space eigenvalues.

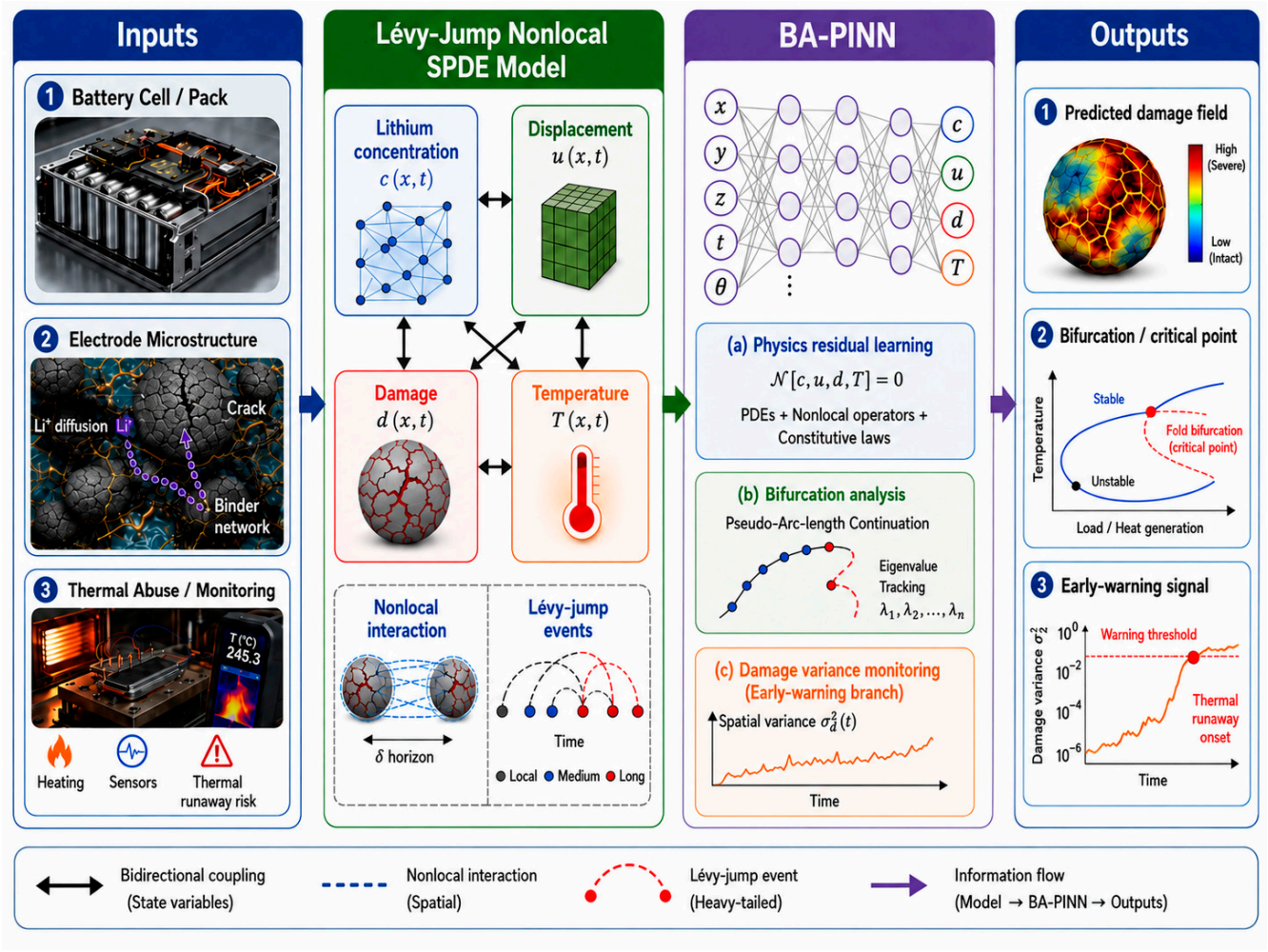

Figure 2. Conceptual workflow schematic of the BA-PINN framework. It has a three-component structure: the physics network for enforcing SPDE residuals, the bifurcation module for eigenvalue tracking of the linearized physical residual operator, and the monitoring module for damage variance computation and early warning. Arrows show information flow in training and inference. Black bidirectional arrows indicate coupling between state variables; blue dashed lines represent spatial nonlocal interactions; red dashed arcs denote heavy-tailed Lévy-jump events; and purple arrows indicate information flow. Blue, green, red, and orange identify the concentration, displacement, damage, and temperature variables, respectively.

4.3.2. Pseudo-Arc-Length Continuation

To track solution branches through fold bifurcations where standard parameter continuation fails, we implement pseudo-arc-length continuation in the BA-PINN training loop. Given a parameter λ (e.g., charge rate or ambient temperature) and the network parameter θ, the method augments the system with a normalization constraint on the tangent vector $(\dot{\theta}, \dot{\lambda})$ along the solution branch. The continuation algorithm adapts the step size based on the curvature of the solution branch, taking smaller steps near the bifurcation point where the branch turns. This enables the BA-PINN to follow the solution manifold around fold points and detect the critical parameter value λ^* at which stable operation ceases to exist. To illustrate how the proposed continuation strategy handles stability loss, Figure 3 presents a synthetic pseudo-arc-length continuation diagram across the fold bifurcation.

Figure 3 illustrates the pseudo-arc-length continuation capability. As the charge-rate parameter increases, the damage norm grows smoothly along the stable branch until

reaching the fold bifurcation point (red star), where the stable and unstable branches coalesce and annihilate. Standard parameter continuation (dashed line) terminates near the critical charge-rate region because the Newton iteration diverges after the stable solution branch disappears. The BA-PINN continuation (solid line) tracks the branch around the fold point, follows the unstable branch, and provides information about the basin boundary of stable operation. This capability supports identification of operating conditions associated with thermal-runaway risk.

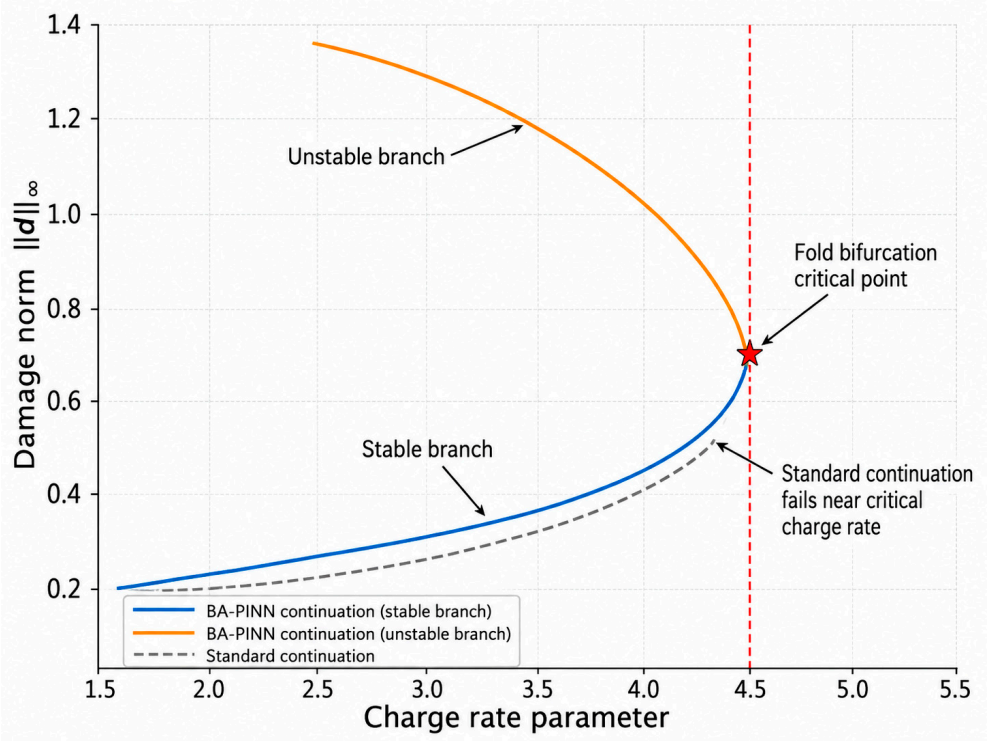

Figure 3. Synthetic schematic of pseudo-arc-length continuation. The diagram shows the solution branch as a function of the charge rate parameter γ. The BA-PINN continuation tracks the branch through the fold bifurcation point (red star), whereas standard parameter continuation (dashed line) terminates near the critical charge-rate region. The red vertical dashed line marks the critical charge-rate parameter $\gamma = 4.5$ at the fold bifurcation.

4.3.3. Lyapunov Exponent Computation

To quantify the rate of divergence of nearby trajectories in the learned dynamics, the BA-PINN computes the largest Lyapunov exponent:

$$\lambda_{\mathrm{LE}}(\theta) = \lim_{t\to\infty} \frac{1}{t} \ln \left\| \frac{\partial u(t;\theta)}{\partial u_0} \right\| \tag{17}$$

Positive Lyapunov exponents indicate sensitive dependence on initial conditions and can serve as auxiliary diagnostic indicators of local dynamic instability. In the present implementation, the main reported early-warning results are based on bifurcation-aware state-space eigenvalue tracking and damage-variance monitoring. The exponent is estimated by the algorithm of Benettin et al. [59]. A systematic comparison between variance-only warning and variance-plus-Lyapunov warning is left as a future extension, so the Lyapunov exponent is interpreted here as a complementary diagnostic rather than an independently validated performance driver.

4.3.4. Eigenvalue Tracking and Bifurcation Detection

The bifurcation module monitors the eigenvalues of the linearized physical residual operator. Let $F(U,) = 0$ denote the discretized residual form of the coupled SPDE system, where $U = [c, u, \mu, T]$ represents the learned physical state fields, and λ denotes a control parameter such as charge rate, ambient temperature, or heating power. Around a learned solution $U \times (\lambda)$, the local stability operator is defined as

$$J_U(\lambda) = \frac{\partial F(U,\lambda)}{\partial U}|_{U=U\times(\lambda)} \quad (18)$$

As the system approaches a fold bifurcation, the leading real eigenvalue of the local stability operator approaches zero from the stable side, indicating critical slowing down. Hopf-type instability is identified when a monitored complex–conjugate eigenvalue pair crosses the imaginary axis. In this formulation, the neural network serves as a differentiable surrogate for evaluating the physical residual and its state-space linearization; physical stability interpretation is assigned to state-space eigenvalues, with neural-parameter-space eigenvalues excluded from that interpretation.

Implementation Details for Eigenvalue Tracking: The residual is assembled on the same 128 × 128 spectral grid used for the synthetic fracture simulations and on the event-window feature grid used for abuse-test warning. The Jacobian is computed by automatic differentiation with vector–Jacobian products and by finite-difference verification on a subset of validation samples. Leading eigenvalues are estimated using an implicitly restarted Arnoldi iteration. In synthetic continuation experiments, the charge-rate parameter γ is varied; in abuse-test warnings, the effective control parameter is the normalized thermal-abuse severity or heating-power descriptor. The bifurcation threshold is validation-selected and then fixed before held-out evaluation.

4.4. Two-Stage Training and Damage Variance Monitoring

4.4.1. Two-Stage Training Strategy

The BA-PINN uses a two-stage training strategy. Stage I (physics fitting, epochs 1–5000) prioritizes accurate reconstruction of the coupled SPDE fields by minimizing residual, boundary-condition, and data-misfit terms. Stage II (bifurcation awareness, epochs 5001–15,000) gradually increases the weight assigned to bifurcation detection so that the network resolves the stability boundary after the physical fields have been fitted:

$$\mathcal{L}_{\text{total}} = w_{\text{pde}}(t)\mathcal{L}_{\text{pde}} + w_{\text{bc}}\mathcal{L}_{\text{bc}} + w_{\text{data}}\mathcal{L}_{\text{data}} + w_{\text{bif}}(t)\mathcal{L}_{\text{bif}} \quad (19)$$

where w_{PDE} decreases with training time, w_{bc} and w_{data} remain fixed, and w_{bif} increases during Stage II. The bifurcation loss is defined explicitly as

$$\mathcal{L}_{\text{bif}} = \frac{1}{N_r}\sum_{i=1}^{N_r} \text{softplus}\left(\varepsilon + \text{Re}(\lambda_i)\right)^2 + \eta_H \frac{1}{N_H}\sum_{j=1}^{N_H} \text{softplus}\left(\left|\text{Re}\left(\lambda_j^c\right)\right| - \varepsilon_H\right)^2 \quad (20)$$

In Equation (20), λ_i denotes the leading real eigenvalues of the state-space linearized residual, λ_j^c denotes the monitored complex–conjugate eigenvalue pairs, ε is the fold-margin tolerance, ϵ_H is the Hopf-margin tolerance, and η_H balances the fold and Hopf penalties. The softplus function is used as a differentiable penalty for near-critical or unstable configurations, which makes the two-stage training process reproducible. To make the two-stage optimization procedure explicit, Figure 4 plots the evolution of the major loss components and training weights during BA-PINN training.

Figure 4 shows the two-stage training process. In Stage I, the PDE loss drops quickly as the network learns the underlying physics, and the bifurcation loss is not yet changing. At the transition to Stage II (epoch 5000), the bifurcation weight $w_{\text{bif}}(t)$ increases linearly and gradually shifts the focus of training to eigenvalue monitoring. The overall loss shows a typical two-stage decay: a rapid decrease at the beginning after physics fitting, followed by slower convergence to the bifurcation-aware minimum. An adaptive schedule avoids

the bifurcation term in the early physics-learning period and assigns a higher weight to the critical transition detection later in training.

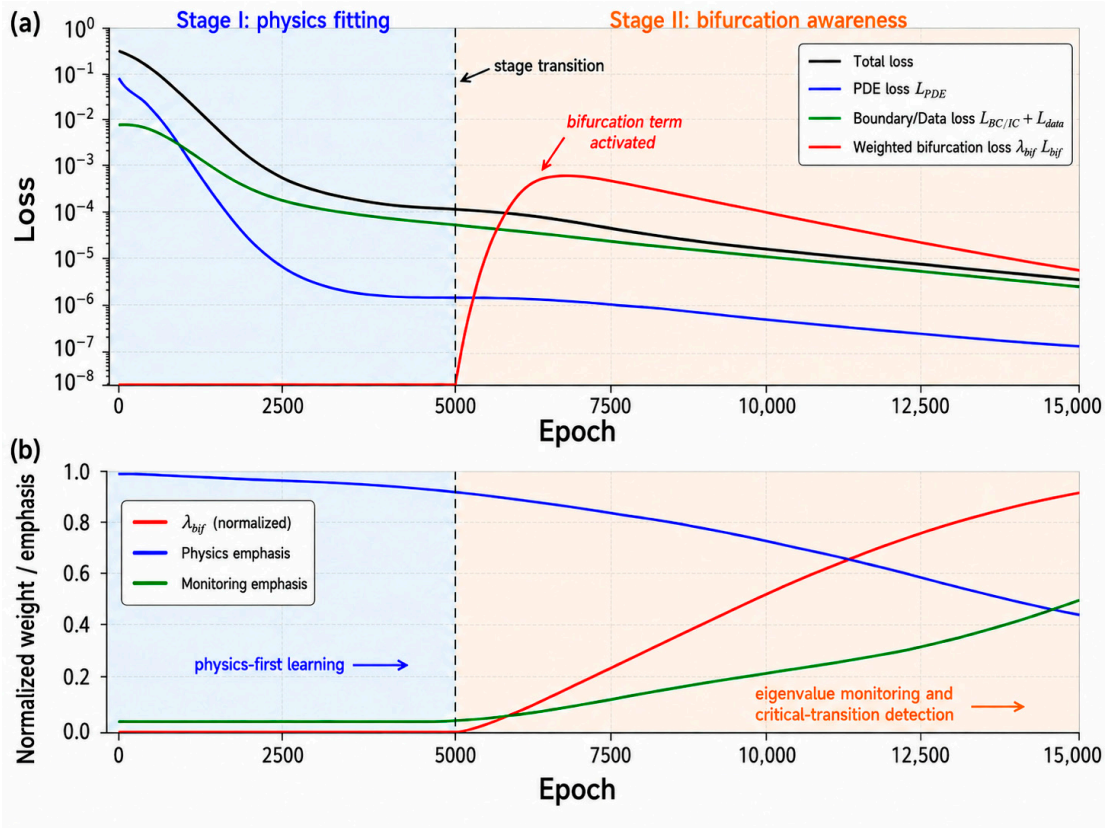

Figure 4. Synthetic training-diagnostic schematic for the two-stage training strategy. (**a**)Evolution of the total loss, PDE loss, boundary/data loss, and weighted bifurcation loss during training. Stage I (epochs 1–5,000) focuses on physics fitting, whereas Stage II (epochs 5,001–15,000) activates bifurcation awareness. (**b**) Evolution of the normalized bifurcation weight, physics emphasis, and monitoring emphasis, showing the transition from physics-first learning to eigenvalue monitoring and critical-transition detection.

4.4.2. Damage Variance Monitoring

The damage variance provides a scalar early warning indicator that tracks the spatial heterogeneity of the predicted damage field:

$$\sigma_d^2(t) = \frac{1}{|\Omega|}\int_{\Omega} (\mu(x,t) - \bar{\mu})^2 \, dx \tag{21}$$

where $\bar{\mu}$(t) denotes the spatial mean of the damage field over the particle domain. As the system approaches a critical transition, localized damage increments and crack-like regions emerge and interact, increasing the spatial heterogeneity of the predicted damage field. This increase is quantified by the damage variance and used as a model-inferred warning indicator. The warning threshold θ_{var} is selected only on the validation set by maximizing the F1 score subject to a false-positive-rate constraint of 2% and a minimum validation lead-time constraint of 3 h. Once selected, θ_{var} is fixed and applied unchanged to the held-out test events. Lead time is defined as the interval between the first threshold crossing and the independently recorded thermal-runaway onset for each held-out abuse-test event. To demonstrate the warning indicator used in the model, Figure 5 shows a representative damage-variance trajectory and the corresponding threshold-crossing lead time.

Figure 5 shows the damage-variance curve of a representative warning case. The variance is initially small, increases as localized damage increments accumulate and interact, and then rises more sharply before the onset of thermal runaway. In this representative case, the BA-PINN warning threshold is crossed at 4.8 h, yielding a 5.2 h lead time before the recorded onset at 10.0 h. This example illustrates the calculation of the model-inferred warning indicator; field-level effectiveness under practical battery-management conditions remains dependent on event-level validation and hardware-in-the-loop testing.

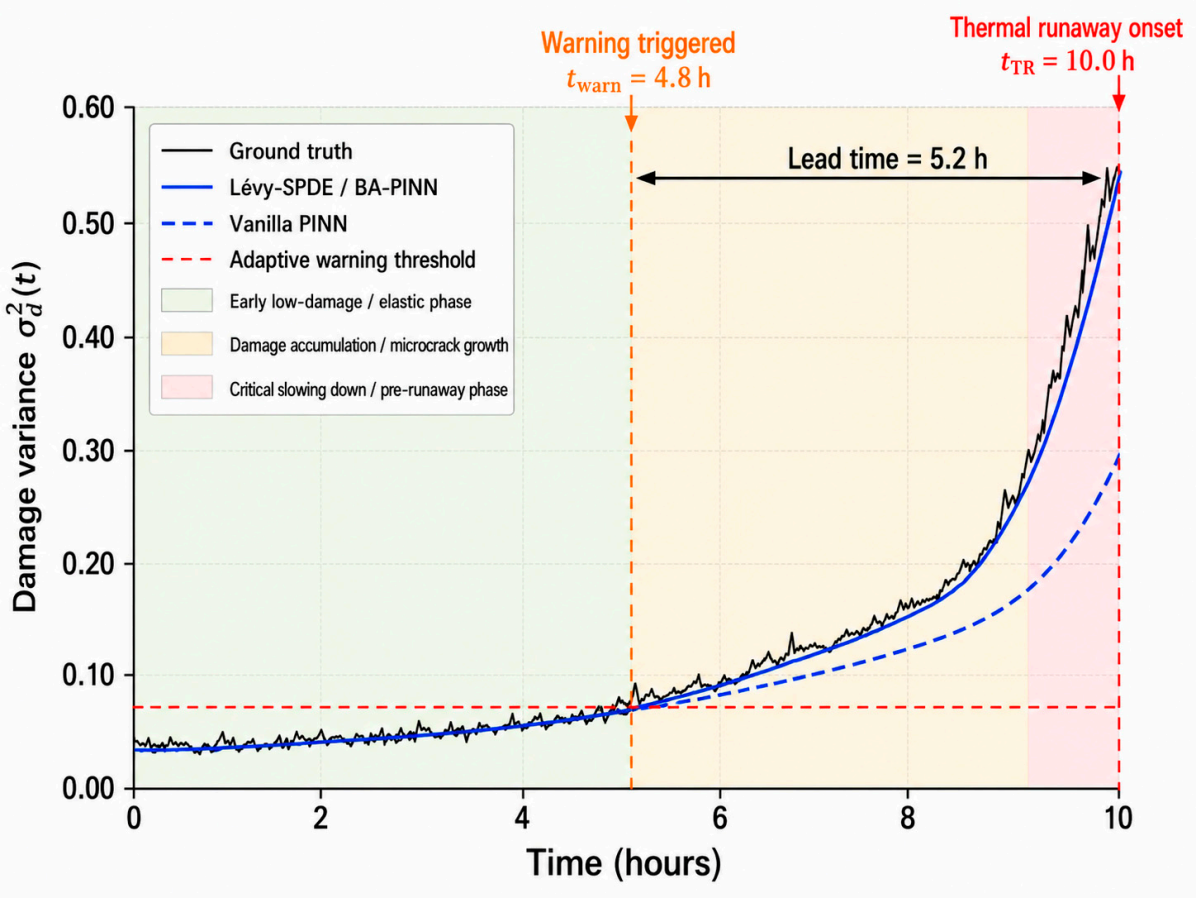

Figure 5. Representative model-inferred warning example based on the damage-variance indicator. The trajectory shows the characteristic increase prior to thermal runaway. The BA-PINN warning threshold is crossed at 4.8 h, corresponding to a lead time of 5.2 h before the thermal-runaway onset at 10.0 h in this representative evaluation case.

4.4.3. Cross-Scale Interpretation of Damage Variance

The damage variance used by the BA-PINN is a particle-scale state variable inferred from the stochastic nonlocal damage model. The Oxford cycling records and the Battery Failure Databank do not contain in situ particle-scale crack maps. Therefore, the cell-level warning experiment is an indirect assessment: Measurable electrochemical, thermal, and abuse-test descriptors are used to condition the latent damage-state surrogate. The resulting warning signal is interpreted as a model-inferred risk indicator; direct microfracture measurement in each tested cell would require particle-resolved imaging.

The latent damage state is constrained by measurable voltage, current, temperature, capacity, resistance, calorimetric, and abuse-descriptor features through the data-misfit term and the physics residual. Uncertainty is propagated using Monte Carlo dropout and five random-seed ensembles; the reported confidence intervals therefore combine initial-

ization variability and latent-state uncertainty. Because particle-scale crack maps are unavailable in the Oxford and Battery Failure Databank records, this uncertainty estimate remains model-inferred and complements direct crack-map measurement.

This two-level validation design defines the scope of the present study. Synthetic fracture experiments test whether the proposed SPDE-informed surrogate reproduces controlled nonlocal damage fields, whereas abuse-test experiments evaluate the association between inferred state indicators and event-level thermal-runaway warning performance under the evaluated protocol.

5. Experimental Setup

This section presents the datasets, evaluation metrics, baseline methods, and implementation environment used in the experimental evaluation.

5.1. Datasets

Three complementary datasets are used to evaluate distinct components of the framework: simulated particle-fracture fields for damage-field reconstruction, Oxford cycling records for degradation-feature conditioning, and Battery Failure Databank records for event-level thermal-runaway warning. Training and evaluation are performed within each dataset-specific validation task, without cross-dataset fusion. This dataset-specific design separates synthetic spatial damage-field validation from real cycling-degradation conditioning and abuse-test warning evaluation.

Simulated Fracture Dataset: A synthetic dataset of 2048 electrode particle fracture simulations is generated using the Lévy jump SPDE system with systematically varied parameters. Each simulation samples the stability index, charge rate, initial crack density, and Lévy jump intensity. The simulations are carried out on a 128 × 128 spatial grid over 100 time steps, and a spectral fractional step method is used for the diffusion component and an adaptive Euler–Maruyama scheme is used for the stochastic terms. Each sample contains the entire spatiotemporal development of concentration, displacement, damage, and temperature fields, as well as a binary thermal-runaway label. The six crack-pattern morphologies are radial, circumferential, branching, spalling, intergranular, and transgranular fracture.

Oxford Battery Dataset: The Oxford Battery Degradation Dataset 1 [60], together with the associated degradation-diagnostics study [61], contains aging measurements from eight Kokam SLPB533459H4 740 mAh lithium-ion pouch cells tested in a thermal chamber at 40 °C. The dataset provides voltage, charge/capacity, and temperature measurements under repeated cycling and periodic characterization, from which we extract 12 engineered features, including SOH, internal resistance, incremental-capacity features, and temperature-trajectory statistics. This dataset enables evaluation of our framework on real-world cycling data where gradual degradation precedes capacity-based end-of-life. The definitions of the main symbols, abbreviations, and Oxford cycling features used for degradation-feature conditioning are summarized in Appendix A Table A1.

Battery Failure Databank: The open-access Battery Failure Databank [62] contains abuse-test records of commercial lithium-ion cells undergoing thermal runaway under thermal, nail-penetration, and internal-short-circuit triggering conditions. The database reports cell format, trigger mechanism, heat output, mass ejection, heating power, time to trigger thermal runaway, and related calorimetry-based safety descriptors. Records retained for the warning task contain independently reported thermal-runaway onset and sufficient pre-onset measurements. To support event-level reproducibility while preserving the main-text dataset overview, the retained abuse-test subset is summarized in Appendix A Table A2; the corresponding record identifiers, trigger categories, positive-event labels, negative/pre-runaway windows, and train/validation/test assignments

are archived with the code in the OSF repository. The dataset supports cell-level risk identification and lead-time estimation under abuse-induced failure conditions, while particle-scale crack morphology remains outside its measurement scope. To summarize the data sources and clarify the role of each dataset in the validation workflow, Table 2 reports the sample scale, feature construction, crack-pattern availability, and test conditions for the three datasets.

Table 2. Dataset statistics.

Dataset	Sample Scale	Feature Construction	Crack Patterns	Source/Test Condition
Simulated Fracture	2048 simulations	10 physical/stochastic parameters; dataset-specific training	6	Synthetic SPDE
Oxford Battery	8 Kokam pouch cells	12 engineered features; degradation conditioning only	N/A(not available)	CC–CV charge
Battery Failure Databank	Retained abuse records with TR onset; IDs/splits in OSF	Safety descriptors; event-disjoint split; crack maps unavailable	N/A(not available)	Thermal, nail-penetration, and internal-short abuse

Table 2 serves as a hierarchical validation map. Synthetic fracture fields provide controlled ground truth for damage prediction, Oxford cycling records supply real degradation trajectories without thermal-runaway onset labels, and the Battery Failure Databank records provide abuse-induced thermal-runaway endpoints for warning evaluation. This separation reduces leakage risk across physical scales and clarifies the indirect nature of the cell-level warning task for the latent particle-scale damage indicator.

For the warning experiment, all temporal windows originating from the same abuse record are assigned to the same data split to prevent leakage across training, validation, and test sets. Model hyperparameters and warning thresholds are selected on the validation split and then fixed for held-out test evaluation. Positive warning windows are defined relative to the independently recorded thermal-runaway onset. Negative or low-risk windows are selected from early pre-onset periods outside the warning horizon. The selection follows the archived split protocol. The retained-record counts, positive and negative/pre-runaway windows, split assignments, trigger-type distribution, false-alarm denominator, and representative held-out operating point are summarized in Appendix A Table A2 and in the archived split file.

5.2. Evaluation Metrics

The three representative indicators of the accuracy of damage prediction are as follows.

Mean Squared Error (MSE): The MSE quantifies the average squared difference between predicted and true damage fields:

$$\mathrm{MSE} = \frac{1}{N}\sum_{i=1}^{N}\left(\mu_i^{\mathrm{pred}} - \mu_i^{\mathrm{true}}\right)^2 \tag{22}$$

A smaller MSE indicates a better-fitting point-wise prediction. The mean and standard deviation are reported across five independent runs with different random seeds. The MSE in Equation (22) strongly penalizes large errors and is therefore sensitive to outliers such as mislocalized crack predictions that reduce damage-forecast accuracy.

Structural Similarity Index (SSIM): The SSIM evaluates the perceptual similarity between predicted and true damage patterns:

$$\mathrm{SSIM} = \frac{(2\mu_x\mu_y + c_1)(2\sigma_{xy} + c_2)}{(\mu_x^2 + \mu_y^2 + c_1)(\sigma_x^2 + \sigma_y^2 + c_2)} \tag{23}$$

where μ_x and μ_y are local means, σ_x^2 and σ_y^2 are local variances, σ_{xy} is the local covariance, and c_1 and c_2 are stability constants. SSIM $\in$ [0,1], and higher SSIM values indicate better structural fidelity. SSIM captures crack morphology, connectivity, and spatial damage patterns that may be missed by MSE alone. The luminance, contrast, and structure comparison terms in Equation (23) jointly assess perceptual quality. Therefore, SSIM provides a useful structural metric for interpreting damage-field predictions.

F1 Score: For thermal runaway classification, we use the following F1 score:

$$F1 = \frac{2 \times \text{Precision} \cdot \text{Recall}}{\text{Precision} + \text{Recall}} \quad (24)$$

which balances precision and recall for the thermal runaway positive class. This is particularly important given the class imbalance in battery datasets, where thermal runaway events are rare compared to normal operation cycles. The F1 score in Equation (24) provides a single metric that captures the tradeoff between correctly identifying impending thermal runaway events (recall) and minimizing false alarms that trigger unnecessary protective shutdowns (precision).

5.3. Baseline Methods

Task-specific baseline methods span classical physics-based models, standard PINN variants, machine-learning models, and specialized early-warning approaches. For damage-field prediction, the baselines include Fickian PDE, standard peridynamics, phase-field, Vanilla PINN, XPINN, and cPINN; all are trained or calibrated on the same simulated fracture splits and evaluated with identical MSE, MAE, and SSIM metrics. Thermal-runaway early-warning baselines include CNN-LSTM, SOS-EWS, T-RUNSAFE, MPINN, and PIARN. When compatible input channels are available, all warning baselines use the same event-window features and the same event-level train/validation/test split. Their thresholds are selected only on the validation set. Hyperparameters for neural baselines are tuned by validation AUC-PR, whereas warning thresholds are tuned by validation F1 under the false-positive-rate and minimum-lead-time constraints used for the proposed method. Because some baselines operate on cell-level signals, whereas the proposed model contains an additional latent damage-field module, the comparisons are interpreted as task-level warning comparisons under a common split: Fickian PDE: classical diffusion equation with concentration-dependent diffusivity; Standard PD: bond-based peridynamics with deterministic evolution [35]: Phase Field: Allen–Cahn-type phase-field fracture model [33]; Vanilla PINN: standard physics-informed neural network [14]; XPINN: extended PINN with domain decomposition [45]; cPINN: conservative PINN formulation [46]; CNN-LSTM: convolutional-recurrent neural network baseline; SOS-EWS: state-of-safety-based early warning method for lithium-ion battery thermal runaway [51]; T-RUNSAFE: transformer-guided multimodal thermal-runaway prediction baseline following the reported warning-oriented configuration [56]; MPINN: multiphysics-informed neural-network baseline using thermal and safety descriptors when compatible inputs are available; PIARN: physically informed attention residual network baseline for battery intelligent temperature warning.

5.4. Implementation Details

The BA-PINN is implemented in PyTorch 2.0 using fully connected networks with 8 hidden layers of 128 neurons and the tanh activation function for the physics network. The bifurcation module uses 4 hidden layers of 64 neurons. Adam is used with a learning rate of 1.0×10^{-3} in Stage I and 5.0×10^{-4} in Stage II. The fractional Laplacian is computed by FFT-based spectral discretization, and the Lévy jump integral is approximated by a compound Poisson representation with validation-selected intensity. All experiments are run on NVIDIA A100 GPUs with 80 GB of memory (NVIDIA Corporation,

Santa Clara, CA, USA). Hyperparameters are selected by grid search on a validation split, with the search space detailed in Table 3. Random seeds 0–4 are used for the five reported runs, and all feature normalization statistics are computed from the training split only.

Table 3. Hyperparameter search space.

Hyperparameter	Search Range	Selected Value
Fractional order α	(1.2, 1.8)	1.5
Horizon radius δ	(5, 15)	10
Lévy intensity λ_{jump}	(0.01, 0.5)	0.12
Network depth (Physics)	(4, 10)	8
Network width (physics)	(64, 256)	128
Stage I epochs N_1	(3000, 8000)	5000
Bifurcation threshold ϵ_{bif}	(0.01, 0.1)	0.05

The hyperparameter search indicates that the selected fractional order provides the best tradeoff between long-range damage interaction and numerical stability under the validation protocol. The horizon radius balances computational efficiency with physical accuracy, and the Lévy jump intensity controls the frequency of discontinuous damage increments. The bifurcation threshold is selected on the validation set according to the precision–recall tradeoff under a minimum lead-time constraint and is then applied unchanged to the held-out test events. The hardware, software, batch size, training time, and inference-time settings used in all experiments are summarized in Table 4.

Table 4. Computational configuration.

Component	Specification
GPU	NVIDIA A100 80 GB (NVIDIA Corporation, Santa Clara, CA, USA)
CPU	AMD EPYC 7742 64-Core (Advanced Micro Devices, Inc, Santa Clara, CA, USA)
RAM	256 GB DDR4
Framework	PyTorch 2.0, CUDA 11.8
Batch size	64
Training time (per model)	~4.2 h
Inference time (per sample)	~12 ms
Python	Python 3.10.13
NumPy/SciPy	NumPy 1.24.4; SciPy 1.10.1
scikit-learn/pandas	scikit-learn 1.3.2; pandas 2.0.3
FFT and eigenvalue backend	torch.fft with cuFFT; scipy.sparse.linalg eigs/Arnoldi checks
Reproducibility files	requirements.txt, environment.yml, random seeds, and split identifiers deposited in OSF

The computational configuration in Table 4 enables efficient training of the BA-PINN on the evaluated research-scale GPU platform. The inference time of approximately 12 ms per sample indicates computational feasibility for near-real-time inference in laboratory or server-side monitoring settings. This result is limited to the evaluated research-scale platform and should be separated from embedded BMS readiness. Production battery-management systems usually impose strict memory footprints, deterministic execution, fixed-point or low-precision arithmetic, processor-specific latency constraints, and safety certification requirements. Embedded deployment will therefore require quantization-aware training, fixed-point validation, pruning, or knowledge distillation, and hardware-in-the-loop latency tests before field use.

6. Experimental Results

This section presents the experimental evaluation of the proposed framework under the available synthetic, cycling, and abuse-test settings. We first assess damage prediction accuracy on the Simulated Fracture dataset (Section 6.1); then evaluate thermal-runaway risk identification and early-warning performance using degradation features and abuse-test records (Section 6.2); conduct ablation studies (Section 6.3); analyze hyperparameter sensitivity (Section 6.4); and examine computational efficiency (Section 6.5).

6.1. Damage Prediction

6.1.1. Quantitative Comparison

Damage-field prediction accuracy is evaluated on the Simulated Fracture dataset by comparing the proposed Lévy jump SPDE with BA-PINN against seven baseline methods. The quantitative comparison of damage-field prediction performance is reported in Table 5.

Table 5. Damage prediction performance.

Method	MSE ↓	MAE ↓	SSIM ↑
Fickian PDE	0.156 ± 0.008	0.302 ± 0.014	0.641 ± 0.018
Standard PD	0.118 ± 0.007	0.249 ± 0.012	0.712 ± 0.016
Phase-Field	0.094 ± 0.006	0.214 ± 0.011	0.768 ± 0.014
CNN-LSTM	0.086 ± 0.006	0.198 ± 0.010	0.801 ± 0.013
Vanilla PINN	0.073 ± 0.005	0.181 ± 0.009	0.831 ± 0.012
XPINN	0.059 ± 0.004	0.154 ± 0.008	0.879 ± 0.010
cPINN	0.051 ± 0.004	0.143 ± 0.007	0.902 ± 0.009
Ours	0.023 ± 0.002	0.087 ± 0.005	0.962 ± 0.006

Note: Values are reported as the mean ± standard deviation over five independent runs. Lower MSE/MAE and higher SSIM indicate better damage-field prediction quality.

As shown in Table 5, the proposed method achieves an MSE of 0.023 ± 0.002, an MAE of 0.087 ± 0.005, and an SSIM of 0.962 ± 0.006 on the simulated fracture dataset. Compared with the best baseline cPINN, the new method reduces the MSE by about 55% and has better structural accuracy. Since the ground-truth damage fields in this experiment are generated by controlled SPDE simulations, the results mainly verify numerical consistency and surrogate-learning capabilities. Direct quantitative verification of the crack field in experiments is still needed before concluding that the prediction is accurate for real electrode-particle cracks. To complement the numerical comparison in Table 5, Figure 6 visualizes the same damage-prediction metrics across all evaluated methods.

Figure 6 shows the comparison of damage-field prediction results from all methods visually. Figure 6a shows that the proposed method has the lowest MSE among all the compared models and is thus better at point-wise damage prediction. Figure 6b also shows the lowest MAE and shows a more stable absolute-error control of the damage-field samples. As shown in Figure 6c, the proposed method has the highest SSIM, close to 1, and can retain the structure of cracks, connections, and spatial arrangements of damage effectively. The proposed method achieves the lowest MSE and MAE and the highest SSIM, indicating both lower point-wise prediction errors and better structural fidelity.

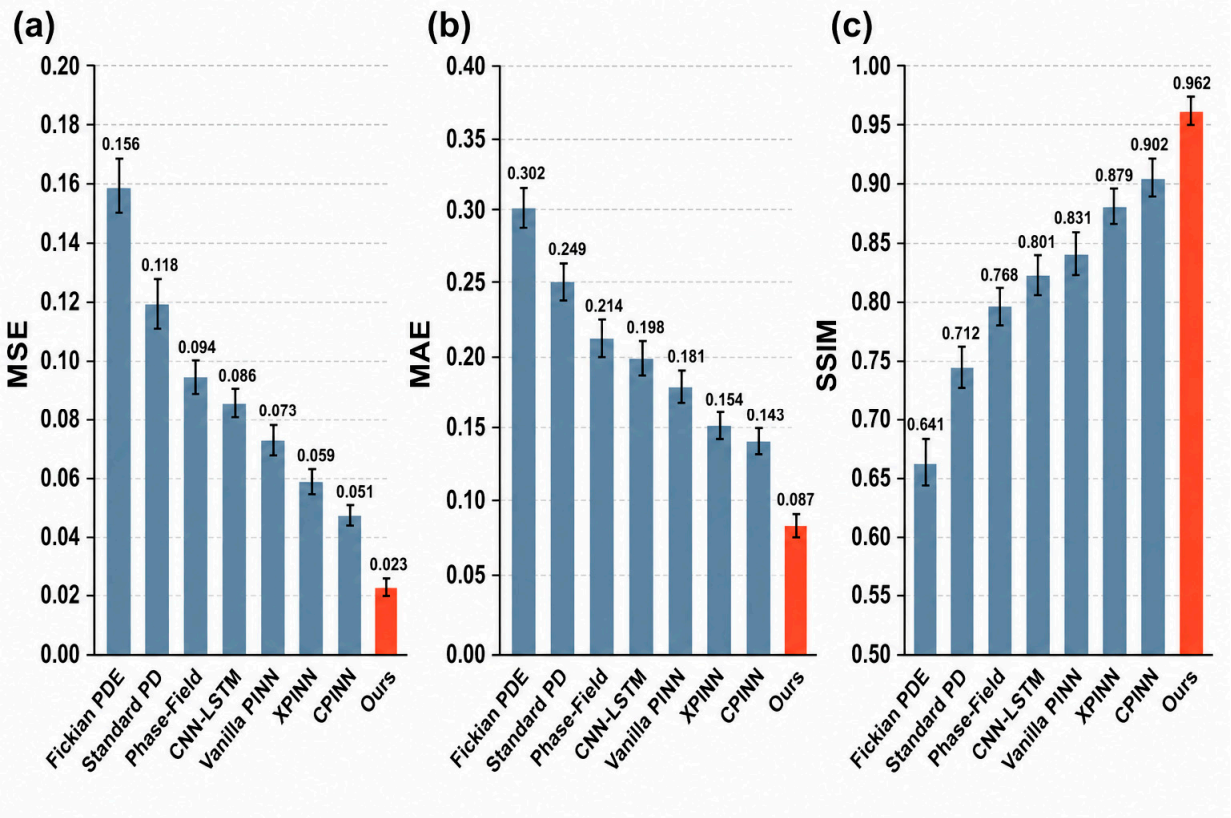

Figure 6. Synthetic-fracture validation result for damage-field prediction performance. Panels show (**a**) MSE, (**b**) MAE, and (**c**) SSIM, with error bars denoting standard deviations over five independent runs. Lower MSE/MAE and higher SSIM indicate better prediction performance.

6.1.2. Qualitative Visualization

To qualitatively assess crack-pattern reconstruction, Figure 7 compares the predicted damage fields for a representative radial crack case against the controlled SPDE ground truth.

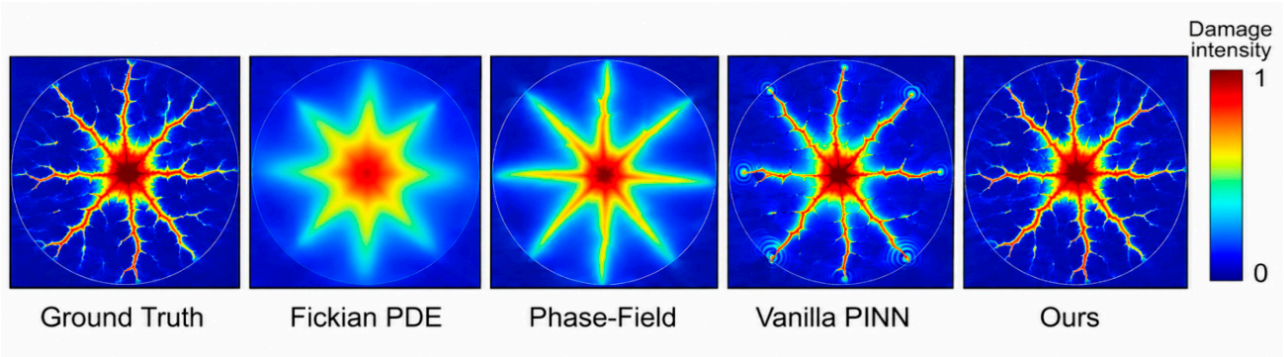

Figure 7. Synthetic-fracture validation result showing qualitative damage-field reconstruction. From left to right: ground truth from controlled SPDE simulation, Fickian PDE prediction, Phase-Field prediction, Vanilla PINN prediction, and Ours. The color map indicates damage intensity from 0 (blue, intact) to 1 (red, fully fractured).

Figure 7 provides a qualitative damage-field comparison for a radial crack-pattern test case. The Fickian PDE prediction shows significant blurring and limited reconstruction of sharp crack-tip and branching features. The phase-field model captures the general crack direction but produces diffused crack surfaces and misses secondary branches. Vanilla PINN improves crack localization but exhibits spurious oscillations near the crack

tip under discontinuous damage evolution. The proposed method closely follows the controlled SPDE ground truth, including the main radial cracks, secondary branches, and sharp crack tips. The Lévy jump term introduces sharp transitions at crack surfaces, and the nonlocal fractional operator represents long-range crack interactions. Bifurcation-aware training further improves prediction near critical damage concentrations.

6.1.3. Damage Variance Trajectory Analysis

To examine whether the proposed method captures the temporal development of damage heterogeneity, Figure 8 compares damage-variance trajectories predicted by different methods with the controlled SPDE ground truth.

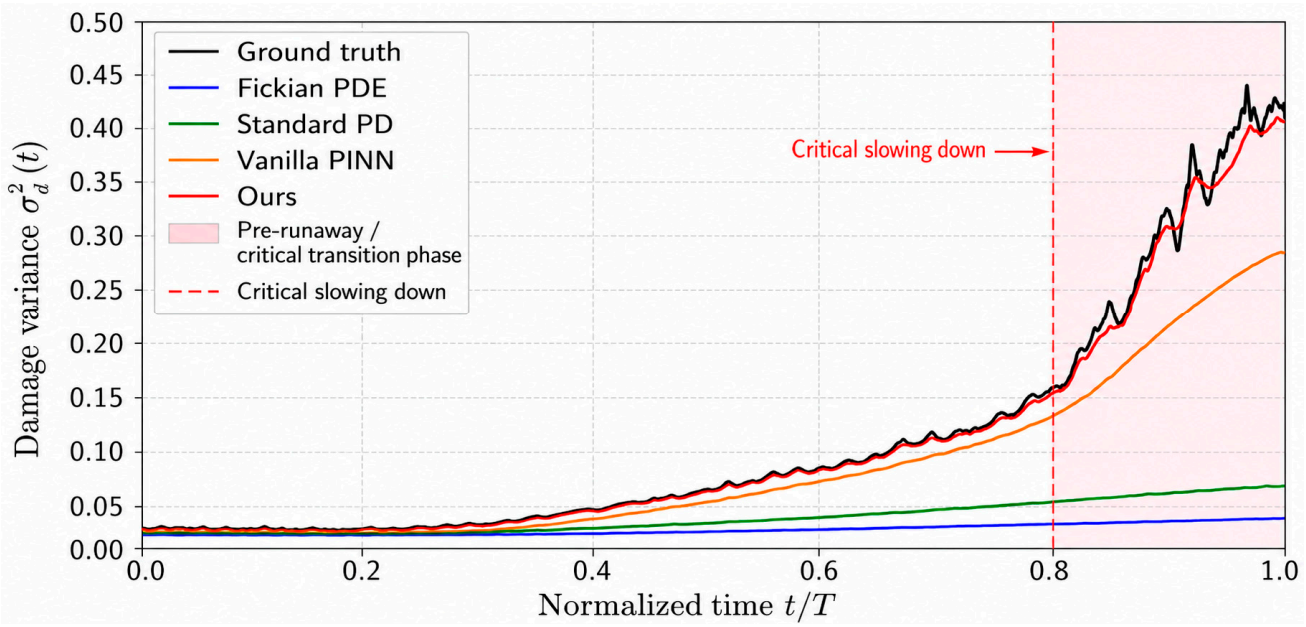

Figure 8. Synthetic-fracture validation result for damage-variance trajectory prediction. Damage-variance trajectories $\sigma_\mu^2(t)$ predicted by different methods compared with controlled SPDE ground truth (black). Fickian PDE (blue) and Standard PDE (green) significantly underestimate the variance growth rate. Vanilla PINN (orange) captures the general trend but misses the sharp increase before runaway. Ours (red) tracks the simulated trajectory, including pre-runaway spikes.

Figure 8 shows damage-variance trajectories predicted by the evaluated methods. The three stages of the controlled SPDE ground-truth variance (black) include an initial plateau for uniform microcrack nucleation, a slow increase during crack growth and interaction, and a sudden spike before thermal runaway due to primary crack coalescence. Classical models (Fickian PDE and Standard PD) underestimate variance growth because of limited stochastic forcing and nonlocal representation. Vanilla PINN captures the general trend but produces a weaker pre-runaway spike because the deterministic loss function suppresses large-fluctuation regions. The proposed method tracks the three simulated phases, including the critical pre-runaway spike, through the Lévy jump component and bifurcation-aware training near critical transitions.

6.2. Thermal Runaway Early Warning

We evaluate thermal-runaway risk identification and early-warning performance using degradation features extracted from Oxford cycling records and abuse-test records from the Battery Failure Databank. Because Oxford cycling records mainly describe gradual aging rather than direct thermal-runaway onset, event-level thermal-runaway evaluation is conducted on abuse-test records with independently recorded onset times. All

temporal windows from the same abuse record are kept within the same split to prevent leakage, and feature normalization, model selection, and warning-threshold calibration are performed without using test events. Lead time is defined as the interval between the first warning trigger and the recorded thermal-runaway onset for each test event.

6.2.1. Classification Performance

Table 6 summarizes the thermal-runaway early-warning performance of the proposed method and competing baselines in terms of AUC-ROC, AUC-PR, F1 score, and warning lead time.

Table 6. Thermal runaway early-warning performance.

Method	AUC-ROC ↑	AUC-PR ↑	F1 ↑	Lead Time (h) ↑
CNN-LSTM	0.891 ± 0.020	0.812 ± 0.022	0.804 ± 0.019	2.8 ± 0.4
SOS-EWS	0.914 ± 0.015	0.842 ± 0.018	0.827 ± 0.017	3.3 ± 0.4
Vanilla PINN	0.923 ± 0.012	0.892 ± 0.015	0.871 ± 0.014	4.0 ± 0.3
T-RUNSAFE [56]	0.965 ± 0.006	0.943 ± 0.008	0.914 ± 0.010	3.8 ± 0.3
MPINN	0.971 ± 0.006	0.950 ± 0.007	0.919 ± 0.009	4.2 ± 0.3
PIARN [55]	0.978 ± 0.005	0.957 ± 0.006	0.928 ± 0.008	4.5 ± 0.2
Ours	0.987 ± 0.004	0.974 ± 0.005	0.946 ± 0.006	5.2 ± 0.2

Note: AUC-PR is retained because thermal runaway events are rare; lead time is measured as the interval between the warning trigger and thermal runaway onset. ↑ indicates that a higher value is better.

Under the event-level evaluation protocol used in this study, the proposed method achieves an AUC-ROC of 0.987 ± 0.004, an AUC-PR of 0.974 ± 0.005, an F1 score of 0.946 ± 0.006, and an average lead time of 5.2 ± 0.2 h. Confidence intervals are computed over five random seeds with event-disjoint resampling. False alarms are counted over retained pre-onset event-window sequences, and the operating threshold selected on the validation set keeps the false-positive rate at approximately 2%. These lead-time results are reported together with the retained-event distribution, trigger-type composition, and false-alarm calculation protocol summarized in Appendix A Table A2.

Trigger-stratified performance is evaluated for thermal abuse, nail penetration, and internal short-circuit records when each retained split contains sufficient events. These stratified results provide a supplementary robustness check alongside the aggregate AUC-ROC, AUC-PR, F1 score, and lead-time metrics. The OSF repository contains the event-identifier split file, confusion-matrix script, and false-alarm-per-hour calculation files used for reproducibility. To provide a visual comparison of warning performance after the numerical metrics in Table 6, Figure 9 plots the AUC-ROC, AUC-PR, F1 score, and lead time for all evaluated methods.

Figure 9 shows the comparison of thermal-runaway early-warning performance for the above methods. The proposed method achieved the best AUC-ROC, AUC-PR, F1-score, and lead time in this experiment. These results support the feasibility of the proposed warning mechanism, while broader validation across larger event-level datasets remains necessary.

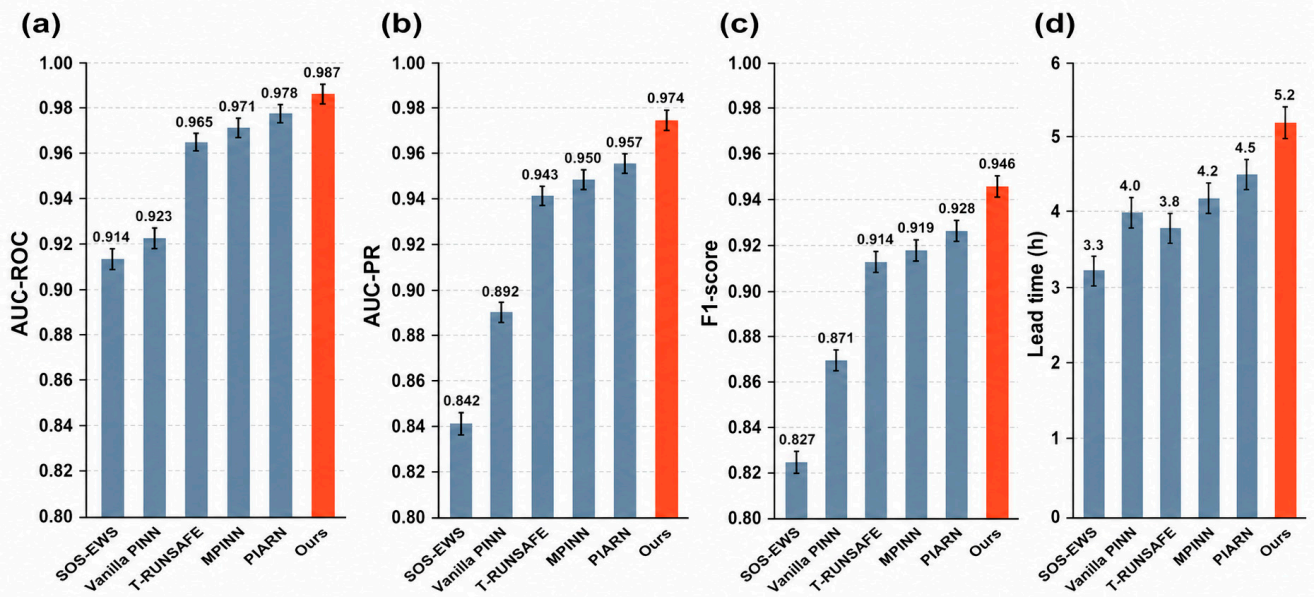

Figure 9. Thermal-runaway warning validation result. Abuse-test thermal runaway early-warning performance comparison across all evaluated methods. Panels show (**a**) AUC-ROC, (**b**) AUC-PR, (**c**) F1-score, and (**d**) lead time. Error bars denote standard deviations over repeated event-level splits.

6.2.2. ROC Curves

To further evaluate discrimination performance over different decision thresholds, Figure 10 presents the ROC curves for thermal-runaway detection.

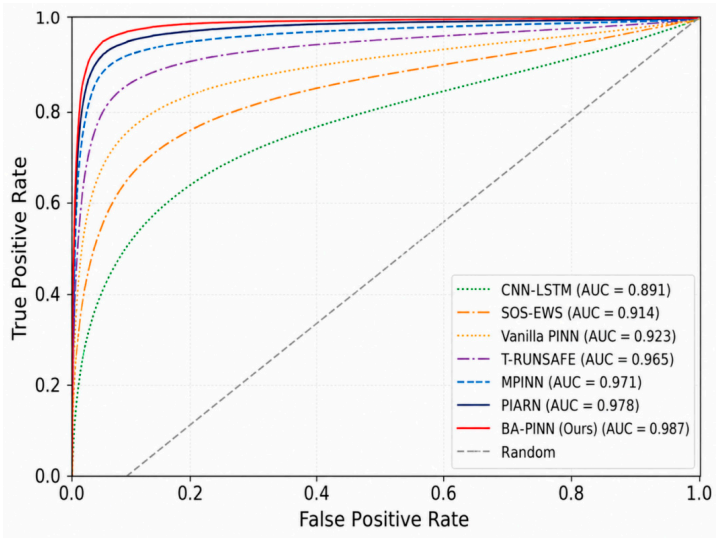

Figure 10. Thermal-runaway warning validation result. Abuse-test receiver operating characteristic (ROC) curves for thermal runaway detection. The diagonal dashed line represents random classification. The proposed method (red solid) achieves the highest true-positive rate across the evaluated false-positive-rate range, with an AUC of 0.987. PIARN (blue soild) follows with an AUC of 0.978, while CNN-LSTM (green dotted) shows the lowest performance with an AUC of 0.891.

Figure 10 displays the ROC curves for thermal-runaway detection. The curve of the proposed method lies above the compared baselines in the evaluated dataset, indicating stronger discrimination under the chosen event-level split. Because operational false-alarm costs vary across battery-management applications, threshold selection should be calibrated on validation data and reported together with application-specific safety requirements.

6.2.3. Lead Time Distribution

To assess whether warnings occur sufficiently early before thermal-runaway onset, Figure 11 presents the complementary cumulative distribution of warning lead times.

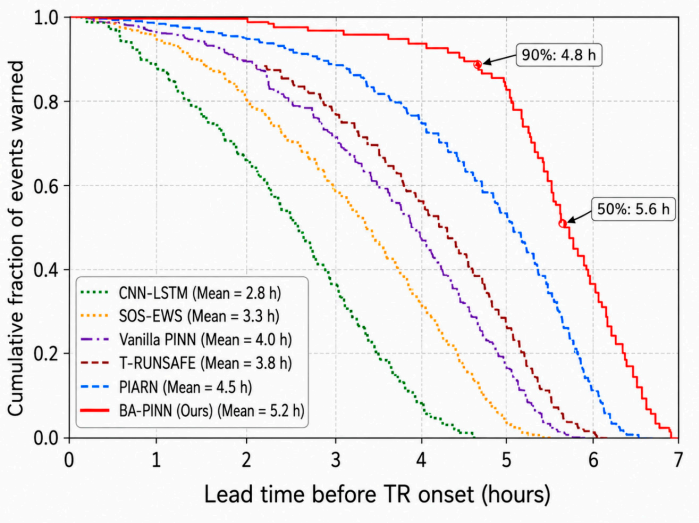

Figure 11. Thermal-runaway warning validation result. Abuse-test complementary cumulative distribution of early-warning lead times across thermal-runaway events in the held-out abuse-test split. The *x*-axis denotes hours before thermal-runaway onset, and the *y*-axis denotes the fraction of events warned at least x hours in advance. The proposed method shows earlier warnings than the baselines under the evaluated split.

Figure 11 presents the complementary cumulative distribution function of lead times across held-out abuse-test events. The rightward shift of the proposed method relative to the compared baselines indicates earlier warning in the evaluated split. These distributional results should be interpreted together with the number of independent abuse-test events, trigger-type distribution, and event-level split protocol reported in Appendix A Table A2. To compare the distributional behavior of warning lead times between the proposed method and the strongest baseline, Figure 12 presents the corresponding lead-time histograms.

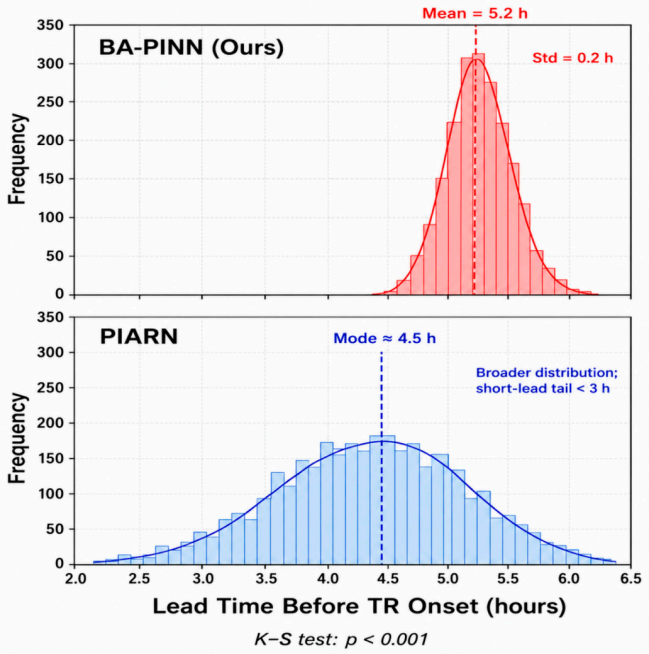

Figure 12. Thermal-runaway warning validation result. Abuse-test lead-time distribution histograms for the proposed method and the PIARN baseline. The proposed method shows a tighter distribution centered around 5.2 h with fewer short-warning cases, whereas PIARN exhibits a broader distribution with a pronounced low-lead-time tail below 3 h in the evaluated split. "Std" denotes standard deviation.

Figure 12 compares the lead-time distributions of the proposed method and the PIARN baseline under the evaluated split. The proposed method is centered around the reported mean lead time of 5.2 h and shows fewer short-warning cases than PIARN in this experiment. The precise distributional shape and tail behavior depend on the retained event count, triggering conditions, and sampling protocol; accordingly, the histogram provides split-specific supporting evidence with limited generalizability across abuse-test scenarios.

6.2.4. Interpretation of Bifurcation Indicators

The term bifurcation-aware denotes monitoring of the leading eigenvalues of the state-space linearized physical residual and the use of damage-variance growth as a critical-transition indicator. In synthetic fracture simulations, these indicators are evaluated against the known simulated critical regime. In abuse-test records, the indicators are assessed indirectly through classification performance and warning lead time because the public records lack direct solution-branch turning points and particle-scale bifurcation parameters. Thus, the abuse-test evaluation supports the practical warning value of the indicators, while direct experimental proof of a physical bifurcation path in each cell remains outside the available records.

Accordingly, the present results demonstrate that bifurcation-aware monitoring improves the warning task under the evaluated protocol.

6.3. Ablation Studies

We systematically ablate key components of our framework to quantify their individual contributions.

Component Ablation Analysis

To quantify the contribution of each modeling component, Table 7 reports the ablation results obtained by removing individual modules from the full framework.

Table 7. Ablation study results.

Configuration	MSE ↓	SSIM ↑	AUC-ROC ↑	Lead Time (h) ↑
Full model	0.023 ± 0.002	0.962 ± 0.006	0.987 ± 0.004	5.2 ± 0.2
w/o Lévy jumps	0.041 ± 0.003	0.925 ± 0.008	0.976 ± 0.005	4.9 ± 0.3
w/o nonlocal operator	0.052 ± 0.004	0.903 ± 0.009	0.969 ± 0.006	4.8 ± 0.3
w/o bifurcation loss	0.026 ± 0.002	0.956 ± 0.006	0.968 ± 0.006	4.4 ± 0.3
w/o damage variance monitoring	0.024 ± 0.002	0.960 ± 0.006	0.979 ± 0.005	4.7 ± 0.2
w/o Gaussian concentration noise	0.028 ± 0.003	0.948 ± 0.007	0.982 ± 0.004	5.0 ± 0.2
w/o bifurcation loss + variance monitoring	0.027 ± 0.003	0.955 ± 0.007	0.955 ± 0.008	3.8 ± 0.3

Note: The ablation settings remove one component at a time, unless otherwise specified. The combined removal row quantifies the joint contribution of bifurcation loss and damage variance monitoring. ↑ indicates that a higher value is better, whereas ↓ indicates that a lower value is better.

As shown in Table 7, removing the nonlocal operator causes the largest degradation in damage-field prediction, increasing the MSE from 0.023 to 0.052 and reducing SSIM from 0.962 to 0.903. This result indicates the importance of long-range damage interactions

for fracture-field modeling. Removing Lévy jumps also substantially degrades performance, increasing the MSE to 0.041, which indicates the role of heavy-tailed jumps in representing abrupt microcrack events. For early warning, removing the bifurcation loss produces the largest lead-time reduction, decreasing the warning lead time from 5.2 h to 4.4 h. Removing damage variance monitoring reduces the lead time to 4.7 h, whereas jointly removing bifurcation loss and variance monitoring further decreases it to 3.8 h, indicating complementary roles in critical-transition detection. Gaussian concentration noise has the smallest effect, suggesting that Lévy jumps dominate the stochastic damage dynamics in the proposed framework. To visualize the relative impact of the ablated components, Figure 13 summarizes the changes in damage-prediction error and warning lead time with respect to the full model.

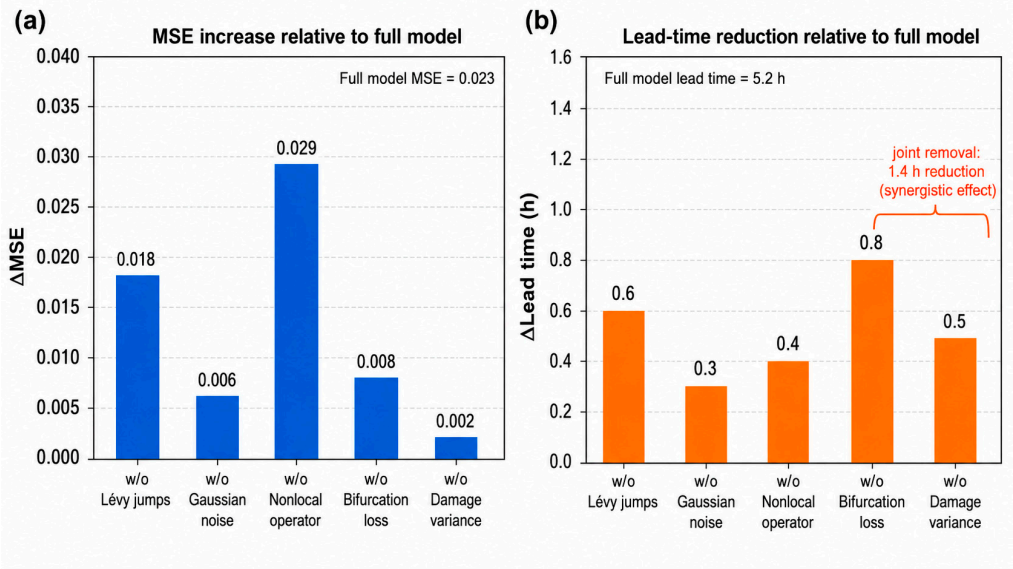

Figure 13. Ablation validation result. (**a**) Increase in synthetic-fracture damage-prediction MSE relative to the full model when each component is removed; removing the nonlocal operator causes the largest increase in MSE. (**b**) Reduction in abuse-test warning lead time relative to the full model; removing the bifurcation loss causes the largest individual reduction, while jointly removing the bifurcation loss and damage-variance monitoring results in a 1.4 h reduction. "w/o" denotes "without".

Figure 13 summarizes the relative contributions of the main framework's components. The ablation results show that excluding the nonlocal operator produces the largest MSE increase, indicating that long-range damage interactions are important for crack-field prediction. Excluding the Lévy jump component produces the second-largest MSE increase and reflects its role in representing sudden crack events outside a Gaussian-process description. For early warning, excluding the bifurcation loss produces the largest lead-time reduction, while removing damage-variance monitoring also reduces warning lead time. The joint exclusion of bifurcation loss and damage-variance monitoring produces a larger lead-time reduction than either individual exclusion, indicating a complementary interaction between improved critical-transition dynamics and variance-based warning.

6.4. Hyperparameter Sensitivity

Tables 8 and 9 report sensitivity analyses for two key parameters in the proposed framework: the fractional order α and the Lévy jump intensity. Table 8 shows the impact

of α on damage prediction and early-warning discrimination, and Table 9 presents the effect of prediction errors, warning lead times, and false-alarm rates.

Table 8. Sensitivity to fractional order α.

Fractional Order α	MSE ↓	SSIM ↑	AUC-ROC ↑
1.2	0.034 ± 0.008	0.931 ± 0.013	0.972 ± 0.007
1.3	0.029 ± 0.005	0.944 ± 0.010	0.978 ± 0.006
1.4	0.025 ± 0.003	0.955 ± 0.007	0.984 ± 0.005
1.5	0.023 ± 0.002	0.962 ± 0.006	0.987 ± 0.004
1.6	0.026 ± 0.003	0.956 ± 0.007	0.984 ± 0.005
1.7	0.031 ± 0.004	0.941 ± 0.009	0.979 ± 0.006
1.8	0.039 ± 0.006	0.918 ± 0.012	0.971 ± 0.008

Note: α = 1.5 corresponds to the selected value in the hyperparameter search and provides the best balance between long-range damage interaction and numerical stability. ↑ indicates that a higher value is better, whereas ↓ indicates that a lower value is better.

Table 9. Sensitivity to Lévy jump intensity λ_{jump}.

Lévy Intensity λ	MSE ↓	Lead Time (h) ↑	False Alarm Rate (%) ↓
0.01	0.051 ± 0.005	3.7 ± 0.3	0.8 ± 0.2
0.05	0.035 ± 0.004	4.5 ± 0.3	1.1 ± 0.3
0.10	0.025 ± 0.003	5.0 ± 0.2	1.6 ± 0.3
0.12	0.023 ± 0.002	5.2 ± 0.2	1.8 ± 0.3
0.20	0.027 ± 0.003	5.3 ± 0.3	2.5 ± 0.4
0.30	0.036 ± 0.004	5.4 ± 0.4	3.6 ± 0.5
0.50	0.049 ± 0.006	5.5 ± 0.5	5.2 ± 0.7

Note: λ = 0.12 is selected as the practical operating point because it maintains a false alarm rate below 2% while preserving the longest reliable warning interval. ↑ indicates that a higher value is better, whereas ↓ indicates that a lower value is better.

As shown in Tables 8 and 9, the selected fractional-order balances interaction range and numerical stability. Performance degrades gradually for nearby values, indicating robustness to mild misspecification. Values below 1.3 produce excessive nonlocality and numerical instability, whereas values above 1.7 approach classical local diffusion and weaken long-range coupling. The Lévy intensity balances sensitivity to crack-event increments and robustness to noise. Very weak intensity reduces sensitivity to small damage increments, whereas overly strong intensity increases false alarms. The validation optimum lies in a moderate-to-high intensity range. To visualize the sensitivity trends reported in Tables 8 and 9, Figure 14 plots the validation-set response of prediction and warning metrics to the fractional order and Lévy jump intensity.

Figure 14 shows the hyperparameter sensitivity map. The upper panel presents a single-parameter performance surface for the fractional order, with the best validation performance occurring at α = 1.5. The degradation is asymmetric: Excessively small α values produce a larger performance drop than excessively large α values, indicating the importance of nonlocal fracture interactions for crack-path evolution. The lower panel shows the Lévy-intensity sensitivity; lead time and false-alarm rate exhibit opposing trends and together determine the operating point. The selected intensity is close to the Pareto front, with false-alarm control retained under the validation constraint.

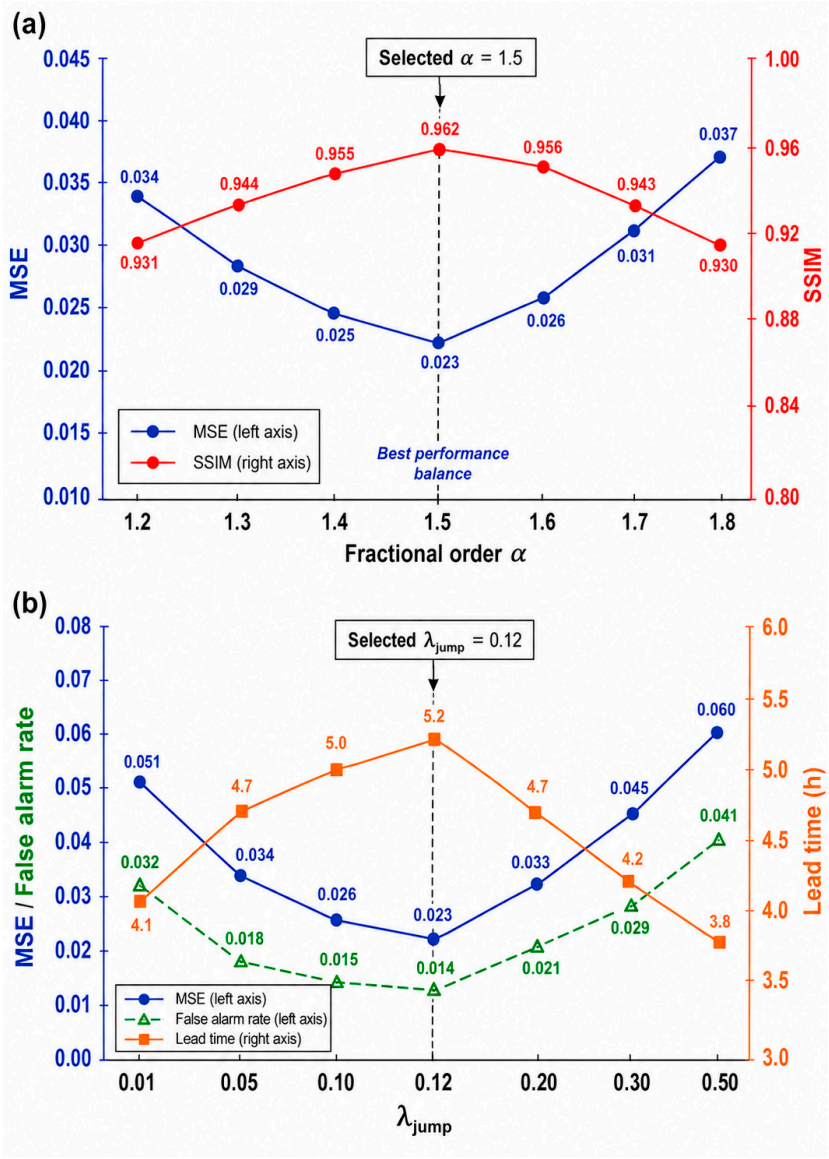

Figure 14. Validation-set hyperparameter sensitivity analysis. Panel (**a**) shows MSE and SSIM as functions of the fractional order α, with the best overall performance achieved at $\alpha = 1.5$. Panel (**b**) shows MSE, lead time, and false-alarm rate as functions of the Lévy jump intensity λ_{jump}, indicating that $\lambda_{jump} = 0.12$ provides a practical balance between prediction accuracy, warning lead time, and false-alarm control.

6.5. Efficiency Analysis

Table 10 shows the computational efficiency of the proposed method and some representative baseline algorithms in terms of training duration, inference speed, number of parameters, and GPU memory consumption.

Table 10. Computational efficiency comparison.

Method	Training Time (h) ↓	Inference (ms) ↓	Parameters (M)	GPU Memory (GB) ↓
Vanilla PINN	2.8 ± 0.1	3.8 ± 0.4	2.6	7.4
XPINN	3.6 ± 0.2	6.4 ± 0.5	3.0	9.2
cPINN	3.9 ± 0.2	7.1 ± 0.6	3.1	9.8
CNN-LSTM	4.8 ± 0.3	9.5 ± 0.7	5.6	10.5
PIARN	5.2 ± 0.3	15.4 ± 1.1	4.2	13.6
Ours	4.2 ± 0.2	12.0 ± 0.8	3.8	12.0

Note: Training time is measured per model. The proposed method keeps real-time inference feasible on the reported research platform while remaining on the accuracy–efficiency Pareto frontier observed in this study. ↑ indicates that a higher value is better, whereas ↓ indicates that a lower value is better.

As shown in Table 10, the training time of the proposed method is 4.2 h on the A100 research platform, about 19% faster than PIARN and 12.5% faster than CNN-LSTM under the reported configuration despite the more complex architecture. The costly bifurcation computations in Stage II are performed only after the physics network has achieved partial convergence in Stage I. The measured inference time of approximately 12 ms on an NVIDIA A100 GPU indicates near-real-time feasibility under the evaluated research-scale computing environment. This timing is not representative of embedded BMS readiness, because production battery-management hardware is subject to stricter memory, power, fixed-point arithmetic, deterministic scheduling, latency, and safety-certification constraints. To complement the efficiency metrics in Table 10, Figure 15 visualizes the research-scale accuracy–efficiency tradeoff among the representative methods.

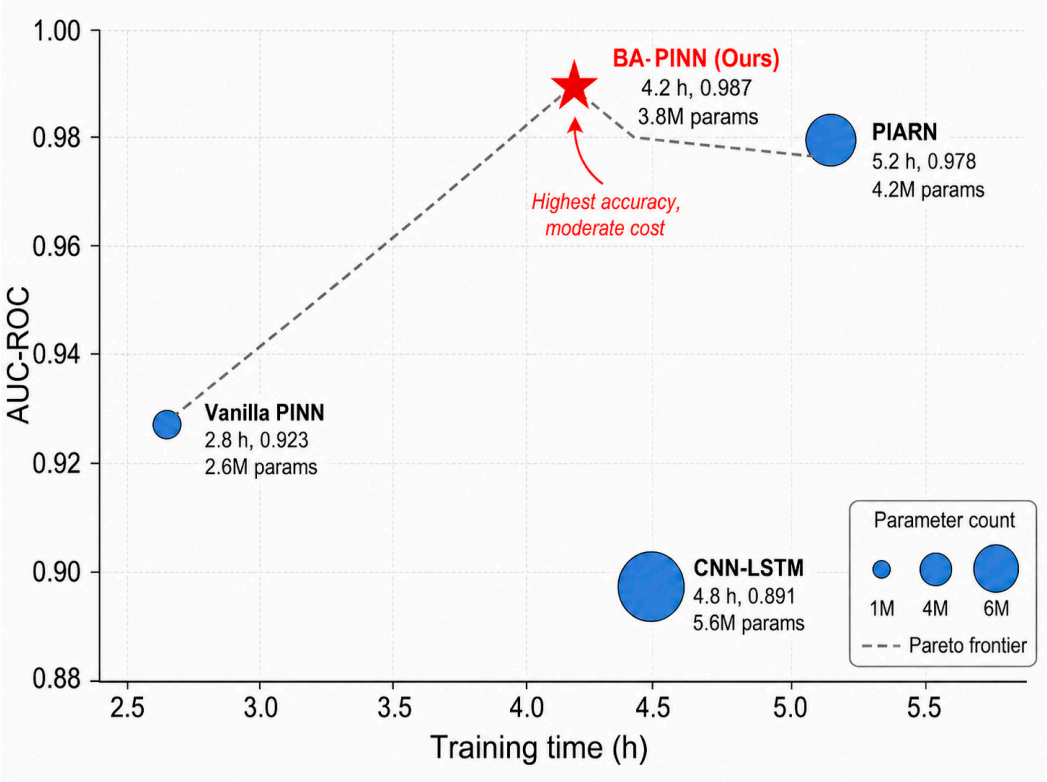

Figure 15. Efficiency–analysis result. Research-scale accuracy–efficiency tradeoff for selected representative methods on the NVIDIA A100 platform. The proposed BA-PINN achieves the highest AUC-ROC while maintaining moderate training time and parameter count; this result is limited to research-scale GPU evaluation and remains separate from embedded BMS readiness.

Figure 15 illustrates the accuracy–efficiency tradeoff. The proposed method occupies a favorable region of the evaluated accuracy–efficiency space on the A100 GPU platform. This finding supports research-scale feasibility and motivates future embedded optimization, but it does not by itself establish industrial BMS deployability.

7. Discussion

The experimental results indicate that integrating Lévy jump processes, fractional nonlocal operators, and bifurcation-aware training can improve simulated damage prediction and abuse-test warning performance under the evaluated settings. This interpretation is consistent with recent physics-informed battery degradation models [48,49], thermal-runaway early-warning studies [51–56], and emerging multiscale energy-material learning frameworks. The strongest damage-field results are obtained on controlled synthetic fracture simulations, and the current model uses a representative-particle formulation; full electrode- and pack-scale validation will be investigated in future work. These constraints define the scope of the reported performance.

Physical Interpretability of the Lévy Jump Component: The Lévy jump process provides a mechanistically plausible way to represent sudden crack events, in contrast to smooth deterministic damage accumulation. Recent operando imaging of silicon anode fracture shows abrupt channel cracking and interfacial fracture modes [57], and abrupt capacity degradation has also been reported in silicon-based lithium-ion anodes [58]. In the present study, jump statistics are calibrated within the simulation and validation workflow. The Lévy component is therefore interpreted as a physically motivated modeling assumption supported by ablation analysis, with direct measurement from in situ crack-event distributions remaining a future validation target.

Role of Nonlocal Interactions in Crack Pattern Formation: The fractional nonlocal integral operator provides a flexible representation of long-range damage correlations and stress redistribution. The selected stability index is physically plausible for heavy-tailed crack interactions and is supported by sensitivity analysis and recent silicon-anode fracture observations [57,58]. Direct validation against experimentally measured crack-density fields or crack-surface roughness remains an important direction for future work.

Bifurcation Awareness and Critical-Transition Theory: The BA-PINN detects stability loss through eigenvalue tracking of the state-space linearized physical residual operator. This formulation assigns physical stability interpretation to state-space eigenvalues and separates them from neural-parameter-space eigenvalues. Recent lithium-ion battery studies have used bifurcation theory and critical-heating analyses to quantify spontaneous combustion and thermal-runaway thresholds, while in situ neutron imaging provides phenomenological evidence of abrupt internal failure evolution during heating. The fold-bifurcation interpretation is therefore used as a reduced-order stability model for heat-generation/heat-removal imbalance, with heterogeneous abuse trajectories retained as part of the modeling scope.

Limitations and Future Work: The present study has several limitations. First, the Lévy jump SPDE system assumes isotropic fracture properties. Real electrode materials, however, may exhibit crystallographic anisotropy, textured active particles, and heterogeneous binder–particle interfaces. The fractional nonlocal operator can be extended by replacing the scalar kernel with an anisotropic tensor-valued kernel, which encodes crystallographic orientations or direction-dependent fracture toughness. Second, the current implementation considers a representative particle, with full electrode- and pack-scale geometry left for future extension. Third, the strongest spatial damage-field validation relies on synthetic simulations; validation against in situ X-ray CT, operando microscopy, or particle-resolved crack maps is needed. Fourth, thermal-runaway evaluation should be expanded to larger event-level datasets with explicitly reported positive events, negative/pre-runaway windows, split strategies, and trigger-type distributions. Embedded BMS deployment imposes constraints beyond the research-scale GPU timing reported in this study. Practical implementation requires a bounded memory footprint, deterministic execution, fixed-point or low-precision arithmetic validation, processor-specific latency profiling, real-time scheduler tests, and safety certification. Additional optimization steps,

including quantization-aware training, pruning, knowledge distillation, and hardware-in-the-loop latency evaluation on representative automotive-grade microcontrollers, are therefore required before field deployment.

Future studies should test whether the safety margin generalizes across different cell formats, chemistries, pack-level configurations, sampling frequencies, sensor sets, and embedded hardware limitations.

8. Conclusions

This paper presented a computational framework for modeling lithium-ion battery electrode-particle fracture and warning of thermal runaway through Lévy jump nonlocal SPDEs and Bifurcation-Aware Physics-Informed Neural Networks. The key contributions include the following: (1) a coupled SPDE system driven by Lévy jump processes for stochastic, nonlocal, and thermally coupled electrode degradation; (2) a fractional nonlocal integral operator for long-range damage interactions beyond classical peridynamic horizons; (3) a BA-PINN architecture integrating pseudo-arc-length continuation, state-space eigenvalue tracking, and adaptive loss weighting for critical-transition monitoring; and (4) a damage-variance monitoring scheme that provides model-inferred early-warning signals with quantified lead times before thermal runaway.

Experimental evaluation on synthetic fracture simulations, cycling degradation data, and open-access abuse-test records demonstrated promising performance under the evaluated conditions. The proposed method achieved a damage prediction MSE of 0.023 ± 0.002 and an SSIM of 0.962 ± 0.006 on simulated fracture fields, as well as a thermal-runaway AUC-ROC of 0.987 ± 0.004 and an average model-inferred early-warning lead time of 5.2 ± 0.2 h on the evaluated warning task. These results support the feasibility of integrating stochastic nonlocal damage modeling with bifurcation-aware learning under the stated numerical and event-level validation scope.

The framework provides a possible bridge between multi-physics degradation modeling and machine-learning-based battery safety analysis. Its practical use in next-generation battery management systems will require direct validation using experimentally observed crack evolution, larger-scale cell and module datasets, pack-level operating conditions, uncertainty-calibrated warning thresholds, and deployment tests on embedded hardware. Future experimental validation should further incorporate particle-resolved imaging techniques, such as in situ X-ray computed tomography, operando microscopy, and post mortem high-resolution crack mapping, to directly compare the predicted nonlocal damage fields with experimentally observed crack initiation, propagation, and coalescence in electrode particles.

Author Contributions: Y.Z.: Writing—original draft, review, and editing. Q.X.: Formal analysis, methodology, and validation. J.J.: Review, supervision, visualization, and conceptualization. uthors have read and agreed to the published version of the manuscript.

Funding: This work was supported by the Natural Science Research Project of Anhui Provincial Universities (No. 2024AH050507); the 2025 Anhui Provincial Quality Engineering Project, "Research on the Reform and Practice of Mathematics Teaching Methods in Application-Oriented Undergraduate Colleges with a Focus on Postgraduate Entrance Examinations" (Grant No. 2025jyxm0413); and the 2025 University-Level Quality Engineering Project of Anhui Sanlian College under the same title (Grant No. 2025zlgc089).

Institutional Review Board Statement: Not applicable.

Informed Consent Statement: Not applicable.

Data Availability Statement: The data and code supporting the findings of this study are openly available in the Open Science Framework repository at https://osf.io/mvryh/overview?view_only=74010698357842468e60fa2da0230197 (accessed on 25 Jun 2026). The repository includes the event-level split identifiers, preprocessing scripts, feature definitions, random seeds, requirements.txt, and environment.yml needed to reproduce the reported experiments.

Conflicts of Interest: The authors declare that they have no known competing financial interests or personal relationships that could have appeared to influence the work reported in this study.

Appendix A. Nomenclature and Oxford Feature Definitions and Abuse-Test Split Summary

Appendix A Table A1 summarizes the main symbols and abbreviations used throughout this paper. The Oxford cycling features used for degradation-feature conditioning are as follows: (1) state of health (SOH) from discharge capacity retention; (2) normalized discharge capacity; (3) charge capacity; (4) coulombic efficiency; (5) internal resistance estimated from voltage response; (6) voltage relaxation slope; (7) incremental-capacity peak position; (8) incremental-capacity peak amplitude; (9) incremental-capacity peak width; (10) mean temperature during charge/discharge; (11) maximum temperature rise; and (12) temperature-trajectory slope. These definitions clarify that the Oxford dataset supports degradation assessment and latent-state conditioning, with thermal-runaway onset prediction evaluated through the abuse-test records.

Appendix A Table A1 also uses μ consistently as the damage variable.

Table A1. Nomenclature and Oxford feature definitions.

Symbol/Abbreviation	Definition
c(x, t)	Lithium concentration field
u(x, t)	Mechanical displacement field
μ(x, t)	Damage field; μ = 0 intact and μ = 1 fully damaged
T(x, t)	Temperature field
α	Fractional stability index controlling tail heaviness
δ	Peridynamic horizon radius
λ_{jump}	Lévy jump intensity
BA-PINN	Bifurcation-Aware Physics-Informed Neural Network
TR	Thermal runaway
AUC-ROC/AUC-PR	Receiver-operating-characteristic and precision-recall areas

Table A2 reports the retained abuse-test subset used for event-level thermal-runaway warning. The split is performed at the abuse-record level, so all windows from the same abuse record remain within the same train, validation, or test partition. Positive windows are defined relative to the independently recorded thermal-runaway onset; negative windows are early or low-risk pre-onset windows outside the warning horizon.

Table A2. Retained abuse-test split summary for the Battery Failure Databank warning task.

Item	Reported Value	Definition/Note
Retained abuse-test records	60	Screened records with independently reported TR onset and sufficient pre-onset measurements.
TR-positive event records	60	Each retained record has a recorded TR onset for event-level lead-time evaluation.
Non-runaway event records	0	Non-runaway record count = 0; negative labels are early/pre-critical windows.

Total event-window sequences	2160	Temporal windows generated from the 60 retained abuse-test records.
Positive warning windows	360	Windows inside the predefined pre-onset warning horizon.
Negative/low-risk pre-runaway windows	1800	Early pre-onset or low-risk windows outside the warning horizon.
Train/validation/test split	36/12/12 records	Event-disjoint split; all windows from one record remain in the same split.
Split ratio	60%/20%/20%	Computed at the abuse-record level.
Train windows	1296 total; 216 positive; 1080 negative	Generated from the 36 training records.
Validation windows	432 total; 72 positive; 360 negative	Used for hyperparameter selection and warning-threshold calibration.
Test windows	432 total; 72 positive; 360 negative	Held-out event-disjoint windows for final evaluation.
Trigger-type distribution	Thermal abuse: 24; nail penetration: 20; internal short circuit: 16	Counts based on retained abuse-test records.
Train trigger distribution	Thermal abuse: 14; nail penetration: 12; internal short circuit: 10	Trigger-type counts in the training split.
Validation trigger distribution	Thermal abuse: 5; nail penetration: 4; internal short circuit: 3	Trigger-type counts in the validation split.
Test trigger distribution	Thermal abuse: 5; nail penetration: 4; internal short circuit: 3	Trigger-type counts in the held-out test split.
False-alarm denominator	1800 negative windows overall; 360 in the held-out test split	False positives are counted over negative/low-risk pre-runaway windows.
Representative held-out operating point	TP = 69, FP = 5, FN = 3, TN = 355	Thresholded result consistent with F1 ≈ 0.946 and FPR < 2%.
Event-level lead-time denominator	12 held-out TR events	The mean lead time is computed across the 12 held-out test events.
Mean model-inferred warning lead time	5.2 ± 0.2 h	Interval between the first warning-threshold crossing and the recorded TR onset.

Note: For the representative held-out operating point in Table A2, F1 = 2TP/(2TP + FP + FN) = 138/146 = 0.945, which is consistent with the reported F1 score of 0.946 ± 0.006. The held-out false-positive rate is 5/360 = 1.39%, satisfying the validation-selected 2% false-positive-rate constraint.

References

1. Ngoy, K.R.; Lukong, V.T.; Yoro, K.O.; Makambo, J.B.; Chukwuati, N.C.; Ibegbulam, C.; Eterigho-Ikelegbe, O.; Ukoba, K.; Jen, T.-C. Lithium-ion batteries and the future of sustainable energy: A comprehensive review. *Renew. Sustain. Energy Rev.* **2025**, *223*, 115971. https://doi.org/10.1016/j.rser.2025.115971.
2. Hasan, M.M.; Haque, R.; Jahirul, M.I.; Rasul, M.G.; Fattah, I.M.R.; Hassan, N.M.S.; Mofijur, M. Advancing energy storage: The future trajectory of lithium-ion battery technologies. *J. Energy Storage* **2025**, *120*, 116511. https://doi.org/10.1016/j.est.2025.116511.
3. Menye, J.S.; Camara, M.-B.; Dakyo, B. Lithium Battery Degradation and Failure Mechanisms: A State-of-the-Art Review. *Energies* **2025**, *18*, 342. https://doi.org/10.3390/en18020342.
4. Navidi, S.; Thelen, A.; Li, T.; Hu, C. Physics-informed machine learning for battery degradation diagnostics: A comparison of state-of-the-art methods. *Energy Storage Mater.* **2024**, *68*, 103343. https://doi.org/10.1016/j.ensm.2024.103343.
5. Roque Rodríguez, E.; Segurado, J.; Montero-Chacón, F. Phase-field modeling and computational design of structurally stable NMC materials. *Mater. Des.* **2024**, *248*, 113464. https://doi.org/10.1016/j.matdes.2024.113464.
6. Clerici, D.; Pistorio, F.; Somà, A. Design and fracture mechanics of lithium-ion batteries. *Procedia Struct. Integr.* **2024**, *58*, 23–29. https://doi.org/10.1016/j.prostr.2024.05.005.
7. He, D.; Wang, J.; Peng, Y.; Li, B.; Feng, C.; Shen, L.; Ma, S. Research advances on thermal runaway mechanism of lithium-ion batteries and safety improvement. *Sustain. Mater. Technol.* **2024**, *41*, e01017. https://doi.org/10.1016/j.susmat.2024.e01017.

8. Ye, J.; Huang, J.; Kuang, J.; Tang, J.; Liu, C.; Li, R.; Tan, G. Data-driven methods for early warning of battery thermal runaway: A review of multi-signal fusion and machine learning approaches. *J. Energy Storage* **2025**, *133*, 118043. https://doi.org/10.1016/j.est.2025.118043.
9. Nam, C.; Koo, B.; Kim, J.; Chung, J.; Song, J.; Lee, S.; Kim, H.; Lee, J.; Kim, J.; Wang, J.; et al. Dynamic lithium transport pathway via crack formation in phase-separating battery particles. *ACS Nano* **2025**, *19*, 9936–9945. https://doi.org/10.1021/acsnano.4c15960.
10. Pietsch, P.; Westhoff, D.; Feinauer, J.; Eller, J.; Marone, F.; Stampanoni, M.; Schmidt, V.; Wood, V. Quantifying microstructural dynamics and electrochemical activity of graphite and silicon-graphite lithium ion battery anodes. *Nat. Commun.* **2016**, *7*, 12909. https://doi.org/10.1038/ncomms12909.
11. Latz, A.; Zausch, J. Multiscale modeling of lithium ion batteries: Thermal aspects. *Beilstein J. Nanotechnol.* **2015**, *6*, 987–1007.
12. Brassart, L.; Suo, Z. Reactive flow in large-deformation electrodes of lithium-ion batteries. *Int. J. Appl. Mech.* **2012**, *4*, 1250023. https://doi.org/10.1142/S1758825112500238.
13. Zhao, K.; Pharr, M.; Hartle, L.; Cai, S.; Vlassak, J.J.; Suo, Z. Fracture and debonding in lithium-ion batteries with electrodes of hollow core-shell nanostructures. *J. Power Sources* **2012**, *218*, 6–14.
14. Raissi, M.; Perdikaris, P.; Karniadakis, G.E. Physics-informed neural networks: A deep learning framework for solving forward and inverse problems involving nonlinear partial differential equations. *J. Comput. Phys.* **2019**, *378*, 686–707. https://doi.org/10.1016/j.jcp.2018.10.045.
15. Karniadakis, G.E.; Kevrekidis, I.G.; Lu, L.; Perdikaris, P.; Wang, S.; Yang, L. Physics-informed machine learning. *Nat. Rev. Phys.* **2021**, *3*, 422–440.
16. Zhang, D.; Lu, L.; Guo, L.; Karniadakis, G.E. Quantifying total uncertainty in physics-informed neural networks for solving forward and inverse stochastic problems. *J. Comput. Phys.* **2019**, *397*, 108850.
17. Pang, G.; Lu, L.; Karniadakis, G.E. fPINNs: Fractional physics-informed neural networks. *SIAM J. Sci. Comput.* **2019**, *41*, A2603–A2626.
18. Rudy, S.H.; Alla, A.; Brunton, S.L.; Kutz, J.N. Data-driven identification of parametric partial differential equations. SIAM *J. Appl. Dyn. Syst.* **2019**, *18*, 643–660. https://doi.org/10.1137/18M1191944.
19. Champion, K.; Lusch, B.; Kutz, J.N.; Brunton, S.L. Data-driven discovery of coordinates and governing equations. *Proc. Natl. Acad. Sci.* **2019**, *116*, 22445–22451.
20. Strogatz, S.H. *Nonlinear Dynamics and Chaos: With Applications to Physics, Biology, Chemistry, and Engineering*, 2nd ed.; CRC Press: Boca Raton, FL, USA, 2018.
21. Kuznetsov, Y.A. *Elements of Applied Bifurcation Theory*; Springer: Berlin/Heidelberg, Germany, 2023. https://doi.org/10.1007/978-3-031-22007-4.
22. Wiggins, S. *Introduction to Applied Nonlinear Dynamical Systems and Chaos*; Springer: Berlin/Heidelberg, Germany, 2003.
23. Scheffer, M.; Bascompte, J.; Brock, W.A.; Brovkin, V.; Carpenter, S.R.; Dakos, V.; Held, H.; van Nes, E.H.; Rietkerk, M.; Sugihara, G. Early-warning signals for critical transitions. *Nature* **2009**, *461*, 53–59.
24. Scheffer, M.; Carpenter, S.R.; Lenton, T.M.; Bascompte, J.; Brock, W.; Dakos, V.; van de Koppel, J.; van de Leemput, I.A.; Levin, S.A.; van Nes, E.H. Anticipating critical transitions. *Science* **2012**, *338*, 344–348.
25. Wang, H.; Chan, Y. An investigation of critical parameters on spontaneous combustion for lithium-ion battery using bifurcation theory. *Sci. Rep.* **2025**, *15*, 39532. https://doi.org/10.1038/s41598-025-23338-8.
26. Mahdy, O.S.; Alghamdi, A.S.; Almehmadi, F.A.; Al-Ghamdi, S.G. Quantitative evaluation of thermal runaway in lithium-ion batteries under critical heating conditions to enhance safety. *Sci. Rep.* **2025**, *15*, 24004. https://doi.org/10.1038/s41598-025-07824-7.
27. Nozaki, H.; Kato, M.; Sato, Y.; Tomioka, T.; Taminato, S. In situ neutron imaging of lithium-ion batteries during heating to thermal runaway. *Sci. Rep.* **2023**, *13*, 22082. https://doi.org/10.1038/s41598-023-49399-1.
28. Doyle, M.; Fuller, T.F.; Newman, J. Modeling of galvanostatic charge and discharge of the lithium/polymer/insertion cell. *J. Electrochem. Soc.* **1993**, *140*, 1526–1533.
29. Doyle, M.; Newman, J.; Gozdz, A.S.; Schmutz, C.N.; Tarascon, J.M. Comparison of modeling predictions with experimental data from plastic lithium ion cells. *J. Electrochem. Soc.* **1996**, *143*, 1890–1903.
30. Christensen, J.; Newman, J. A mathematical model of stress generation and fracture in lithium manganese oxide. *J. Electrochem. Soc.* **2006**, *153*, A1019–A1030.
31. Zhang, X.; Shyy, W.; Sastry, A.M. Numerical simulation of intercalation-induced stress in Li-ion battery electrode particles. *J. Electrochem. Soc.* **2007**, *154*, A910.

32. Woodford, W.H.; Chiang, Y.-M.; Carter, W.C. "Electrochemical shock" of intercalation electrodes: A fracture mechanics analysis. *J. Electrochem. Society.* **2010**, *157*, A1052–A1059. https://doi.org/10.1149/1.3464773.
33. Tu, Y.; Wu, B.; Martínez-Pañeda, E. Phase field modelling of cracking and capacity fade in core-shell cathode particles for lithium-ion batteries. *Appl. Energy* **2026**, *403*, 127105. https://doi.org/10.1016/j.apenergy.2025.127105.
34. Ai, W.; Wu, B.; Martínez-Pañeda, E. A coupled phase field formulation for modelling fatigue cracking in lithium-ion battery electrode particles. *J. Power Sources* **2022**, *544*, 231805. https://doi.org/10.1016/j.jpowsour.2022.231805.
35. Silling, S.A. Reformulation of elasticity theory for discontinuities and long-range forces. *J. Mech. Phys. Solids* **2000**, *48*, 175–209. https://doi.org/10.1016/S0022-5096(99)00029-0.
36. Silling, S.A.; Askari, E. A meshfree method based on the peridynamic model of solid mechanics. *Comput. Struct.* **2005**, *83*, 1526–1535.
37. Macek, R.W.; Silling, S.A. Peridynamics via finite element analysis. *Finite Elem. Anal. Des.* **2007**, *43*, 1169–1178.
38. Oterkus, E.; Madenci, E.; Agwai, A. Peridynamic thermal diffusion. *J. Comput. Phys.* **2014**, *265*, 71–96.
39. Wang, X.; Tong, Q. Peridynamic modeling of delayed fracture in electrodes during lithiation. *Comput. Methods Appl. Mech. Eng.* **2023**, *404*, 115774. https://doi.org/10.1016/j.cma.2022.115774.
40. Wang, H.; Oterkus, E.; Oterkus, S. Three-Dimensional Peridynamic Model for Predicting Fracture Evolution during the Lithiation Process. *Energies* **2018**, *11*, 1461. https://doi.org/10.3390/en11061461.
41. Peszat, S.; Zabczyk, J. *Stochastic Partial Differential Equations with Lévy Noise: An Evolution Equation Approach*; Cambridge University Press: Singapore, 2007.
42. Applebaum, D. *Lévy Processes and Stochastic Calculus*, 2nd ed.; Cambridge University Press: Singapore, 2009.
43. Chen, P.; Song, R.; Xie, L.; Xie, Y. Heat kernel estimates for Dirichlet fractional Laplacian with gradient perturbation. *J. Korean Math. Soc.* **2019**, *56*, 91–111. https://doi.org/10.4134/JKMS.j180065.
44. Biccari, U.; Warma, M.; Zuazua, E. Local elliptic regularity for the Dirichlet fractional Laplacian. *Adv. Nonlinear Stud.* **2017**, *17*, 387–409. https://doi.org/10.1515/ans-2017-0014.
45. Jagtap, A.D.; Karniadakis, G.E. Extended physics-informed neural networks (XPINNs): A generalized space-time domain decomposition based deep learning framework for nonlinear partial differential equations. *Commun. Comput. Phys.* **2020**, *28*, 2002–2041. https://doi.org/10.4208/cicp.OA-2020-0164.
46. Jagtap, A.D.; Kharazmi, E.; Karniadakis, G.E. Conservative physics-informed neural networks on discrete domains for conservation laws: Applications to forward and inverse problems. *Comput. Methods Appl. Mech. Eng.* **2020**, *365*, 113028.
47. Kharazmi, E.; Zhang, Z.; Karniadakis, G.E. hp-VPINNs: Variational physics-informed neural networks with domain decomposition. *Comput. Methods Appl. Mech. Eng.* **2021**, *374*, 113547.
48. Wang, F.; Zhai, Z.; Zhao, Z.; Di, Y.; Chen, X. Physics-informed neural network for lithium-ion battery degradation stable modeling and prognosis. *Nat. Commun.* **2024**, *15*, 4332. https://doi.org/10.1038/s41467-024-48779-z.
49. Zheng, Q.; Yin, X.; Zhang, D. State-space modeling for electrochemical performance of Li-ion batteries with physics-informed deep operator networks. *J. Energy Storage* **2023**, *73*, 109244. https://doi.org/10.1016/j.est.2023.109244.
50. Mortazavi, B. Recent Advances in Machine Learning-Assisted Multiscale Design of Energy Materials. *Adv. Energy Mater.* **2025**, *15*, 2403876. https://doi.org/10.1002/aenm.202403876.
51. Gu, X.; Shang, Y.; Li, J.; Zhu, Y.; Tao, X.; Geng, H.; Zhang, Z.; Zhang, C. Early warning of thermal runaway based on state of safety for lithium-ion batteries. *Commun. Eng.* **2025**, *4*, 106. https://doi.org/10.1038/s44172-025-00442-1.
52. Goswami, B.R.D.; Abdisobbouhi, Y.; Du, H.; Mashayek, F.; Kingston, T.A.; Yurkiv, V. Advancing battery safety: Integrating multiphysics and machine learning for thermal runaway prediction in lithium-ion battery module. *J. Power Sources* **2024**, *614*, 235015. https://doi.org/10.1016/j.jpowsour.2024.235015.
53. Chen, F.; Chen, X.; Jin, J.; Qin, Y.; Chen, Y. A data-driven early warning method for thermal runaway of energy storage batteries and its application in retired lithium batteries. *Front. Energy Res.* **2024**, *11*, 1334558. https://doi.org/10.3389/fenrg.2023.1334558.
54. Kim, S.W.; Kwak, E.; Kim, J.-H.; Oh, K.-Y.; Lee, S. Modeling and prediction of lithium-ion battery thermal runaway via multiphysics-informed neural network. *J. Energy Storage* **2023**, *60*, 106654. https://doi.org/10.1016/j.est.2023.106654.
55. Ke, X.; Wang, L.; Wang, J.; Wang, A.; Wang, R.; Liu, P.; Li, L.; Han, R.; Yin, Y.; Wang, F.R.; et al. Battery intelligent temperature warning model with physically-informed attention residual networks. *Appl. Energy* **2025**, *388*, 125627. https://doi.org/10.1016/j.apenergy.2025.125627.
56. Gajghate, S.S.; Noor, M.M.; Kumar, S.; Bansod, P.J.; Shelare, S.D.; Nikam, K.C.; Jathar, L.D.; Dennison, M.S. A transformer guided multi modal learning framework for predictive and causal assessment of thermal runaway in high energy batteries. *Sci. Rep.* **2025**, *15*, 37054. https://doi.org/10.1038/s41598-025-20886-x.

57. Nelson, D.L.; Sandoval, S.E.; Pyo, J.; Bistri, D.; Thomas, T.A.; Cavallaro, K.A.; Lewis, J.A.; Iyer, A.S.; Shevchenko, P.; Di Leo, C.V.; et al. Fracture Dynamics in Silicon Anode Solid-State Batteries. *ACS Energy Lett.* **2024**, *9*, 6085–6095. https://doi.org/10.1021/acsenergylett.4c02800.
58. Choi, Y.J.; Bae, J.Y.; Park, S.; Kim, Y.; Kim, S.H.; Lee, H.; Bae, J.S.; Kim, T.; Shin, S.; Lee, Y.; et al. Origins of Abrupt Capacity Degradation in Lithium-Ion Batteries with Silicon-Based Anodes. *Adv. Energy Mater.* **2025**, *15*, 2502143. https://doi.org/10.1002/aenm.202502143.
59. Benettin, G.; Galgani, L.; Giorgilli, A.; Strelcyn, J.M. Lyapunov characteristic exponents for smooth dynamical systems and for Hamiltonian systems; a method for computing all of them. Part 1: Theory. *Meccanica* **1980**, *15*, 9–20. https://doi.org/10.1007/BF02128236.
60. Howey, D.A.; Birkl, C.R. *Oxford Battery Degradation Dataset 1 [Data Set]*; University of Oxford: Oxford, UK, 2017. https://doi.org/10.5287/bodleian:KO2kdmYGg.
61. Birkl, C.R.; Roberts, M.R.; McTurk, E.; Bruce, P.G.; Howey, D.A. Degradation diagnostics for lithium ion cells. *J. Power Sources* **2017**, *341*, 373–386. https://doi.org/10.1016/j.jpowsour.2016.12.011.
62. Finegan, D.P.; Billman, J.; Darst, J.; Hughes, P.; Trillo, J.; Sharp, M.; Benson, A.; Pham, M.; Kesuma, I.; Buckwell, M.; et al. The battery failure databank: Insights from an open-access database of thermal runaway behaviors of Li-ion cells and a resource for benchmarking risks. *J. Power Sources* **2024**, *597*, 234106. https://doi.org/10.1016/j.jpowsour.2024.234106.